Chapter 5
Solid State Detectors

G. Lutz and R. Klanner

5.1 Introduction

Semiconductor detectors, and in particular silicon detectors, are very well suited for detection and measurement of light and of ionizing radiation caused by interaction with charged particles and (X-ray) photons. Precise position, time and energy measurement can be combined when use is made of the excellent intrinsic material properties in well thought out detector concepts.

Development and large scale use of silicon detectors has been initiated by particle physics. The discovery of the rare and short lived charmed particles lead to the desire to use their decay topology as signature for identification and separation from non-charm background. Detectors were required that combined very good position measurement (in the range of several μm) with high rate capability (few hundred kHz), a task not achievable with available detectors at that time.

Semiconductor detectors, in particular silicon and germanium detectors were used for quite some time, but not too frequently, in Nuclear Physics for the

---

In the updated version a number of detector developments which took place after the publication of the original version have been taken into account. These are in particular new sections on Radiation Damage, 3-D Detectors, MAPS (Monolithic Active Pixel Sensors), SiPMs (Silicon Photomultipliers) and Ultrafast Tracking Detectors (LGAD = Low Gain Avalanche Detectors). In addition, the section Summary and Outlook has been updated.

The author G. Lutz is deceased at the time of publication.

G. Lutz
PNSensor GmbH and MPI-Halbleiterlabor, Munich, Germany

R. Klanner (✉)
Department of Physics, University of Hamburg, Hamburg, Germany
e-mail: robert.klanner@desy.de

purpose of measuring particle and X-ray photon energies, not however for position measurement. This task was left mostly to gas detectors and to scintillation hodoscopes, both of them not able to provide the required position measurement resolution.

It was realized rather soon that semiconductors offer in principle the required capabilities and silicon strip detectors were developed and used for the detection and investigation of charmed particles. This development rapidly increased in speed and scope so that today it is rare to find particle physics experiments that do not rely heavily on silicon strip detectors for particle tracking and identification. Strip detectors have also entered many other fields of science. Important features of this development were the introduction of more sophisticated detector concepts and the development of multi-channel low noise-low power integrated readout electronics adapted to the requirements of strip detectors.

A further challenge in particle tracking poses the ambiguities occurring in case of high particle densities. This problem is alleviated considerably when replacing the strip geometry by pixels. Hybrid pixel detectors became possible with the enormous progress in miniaturization of electronics. Each pixel has its own readout channel. Detector and electronics with matched geometry are connected face to face by bump bonding. Recently Monolithic Active Pixel Sensors (MAPS), pixel detectors in which sensor and readout electronics are integrated on the same silicon chip, are reaching maturity.

Although in the initial phase of this rapid development position measurement was in the focus of interest, energy resolution with high readout speed came back to its right, sometimes in combination with position resolution. This development opened the door of semiconductor detectors in X-ray astronomy, synchrotron radiation experiments and in many other fields.

A major step on this way was the invention by E. Gatti and P. Rehak of the semiconductor drift chamber [1]. This concept also became the basis for further new concepts as are the pnCCD [2], the silicon drift diode [3] and the DEPFET [3] that forms the basis for several types of pixel detectors with rather unique properties.

In the last decade, a major progress in the field of silicon photo-detectors took place: Multi-pixel avalanche photo diodes operating in the Geiger mode, frequently called silicon photo-multipliers, SiPM, have been developed and found many applications in research, medicine and industry.

In the following, detection principles and properties of the various detector types will be described and some applications will be sketched. Emphasis is on detector physics and concepts while it is impossible to cover all important activities in the field. In addition, a short summary of radiation damage, which presents a major challenge for the use of silicon detectors in the harsh radiation environment at colliders, like at the CERN Large Hadron Collider, LHC, will be presented.

5.2 Basic Detection Process of Single Photons in Semiconductors

The simplest detector is a reverse-biased planar diode (Fig. 5.1). Photons interacting in silicon will, dependent on their energy, produce one or more electron-hole pairs close to their points of interaction. Charged particles will generate pairs along their path within the semiconductor. An average energy of 3.6 eV is needed for creation of a pair in silicon with a band gap of 1.12 eV at room temperature. This should be compared with the ionization energy of gases which is more than an order of magnitude higher. Electrons and holes will be separated by the electric field within the space charge region and collected at the electrodes on opposite sides of the diode.

The small band gap and the corresponding large signal charge generated in the photon absorption process is the principal cause for the excellent properties of semiconductor radiation detectors manifesting themselves in particular in very good spectroscopic resolution down to low energies. Further reasons are the high density and corresponding low range of delta-electrons which makes very precise position measurement possible. High charge carrier mobilities combined with small detector volume leads to short charge collection time and makes the use of detectors in high rate environment possible. The excellent mechanical rigidity makes the use of gas containment foils superfluous and allows operation in the vacuum. Therefore very thin entrance windows can be constructed and high quantum efficiency can be reached down to low photon energies. Position dependent doping of semiconductors allows construction of detectors with sophisticated electric field configurations and intrinsically new properties.
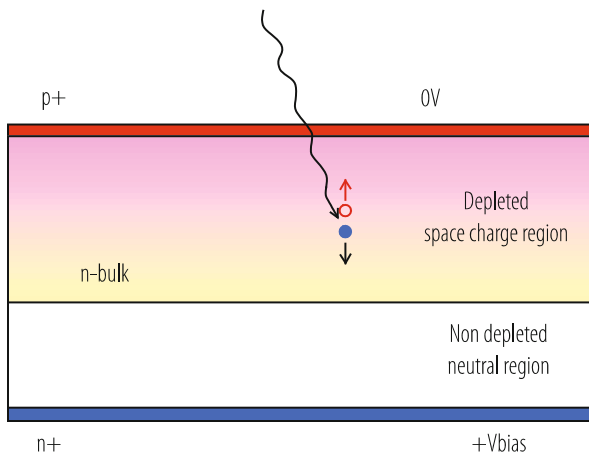
Fig. 5.1 Schematic structure of a reverse-biased semiconductor diode used as photon detector. The region heavily doped with acceptors is denoted p^+, and n-bulk and n^+ the regions lightly and heavily doped with donors, respectively

Reaching all these good detector properties requires a readout electronics which is well matched to the detectors. Here we notice a point specific to silicon which is also the basic material of most of present day electronics. For that reason it is natural to integrate the sensitive front-end part of electronics into the detector. This is the case, for example, in CCDs and drift diodes [3] with very high spectroscopic resolution. A further device (DEPFET) [3] combines the function of detector and amplifier in the basic structure. In MAPS (Monolithic Active Pixel Sensors) sophisticated readout electronics is directly integrated on the silicon chip of the sensor.

Dependent on the field of application different aspects of semiconductors are in the focus of interest. In particle physics tracking requires high position resolution and often high speed capabilities while energy resolution is of less importance. Recently at the CERN LHC also a timing accuracy of a few tens of picoseconds in combination with precision tracking became a requirement. In X-ray spectroscopy and imaging, as well as in X-ray astronomy both energy and position resolution are of importance. For light detection, high photon-detection efficiency and resolving single photons are typically more important than position accuracy.

5.3   Basics of Semiconductor Physics

After these introductory remarks on semiconductor detectors we will look into the underlying mechanisms in a little more detail.

Most commonly used semiconductors are single crystals with diamond (Si and Ge) or zinc blende (GaAs and other compound semiconductors) lattice. Each atom in the crystal shares their outermost (valence) electrons with the four closest neighbours. At very low temperature all electrons are bound to their respective locations and the material is an insulator. At elevated temperature thermal vibrations will sometimes break a bond and both the freed electron and the hole (the empty place left behind to be filled by a neighbouring electron) are available for electrical conduction. The density of free electrons/holes is called intrinsic carrier density n_i. For silicon its value at room temperature is about 10^{10} cm^{-3}, resulting in an intrinsic resistivity of about 350 kΩ·cm.

Creation of electron–hole pairs can also be accomplished by electromagnetic radiation or by the passage of charged particles knocking out of their covalent bond some of the valence electrons. This is the mechanism used in the detection process. These free charge carriers will then be moved by an applied electrical field (drift) and redistribute due to concentration variations (diffusion) until finally reaching an external electrode connected to the readout electronics.

So far we have only dealt with intrinsic semiconductors, perfect crystals without foreign atoms. One may, however, replace a small fraction of atoms with some having either one more, called donors (e.g. P in Si) or one less, called acceptors (e.g. B in Si) valence electron. The additional electron or the missing electron (hole) is only weakly bound, resulting in states in the silicon band gap located about 40 meV
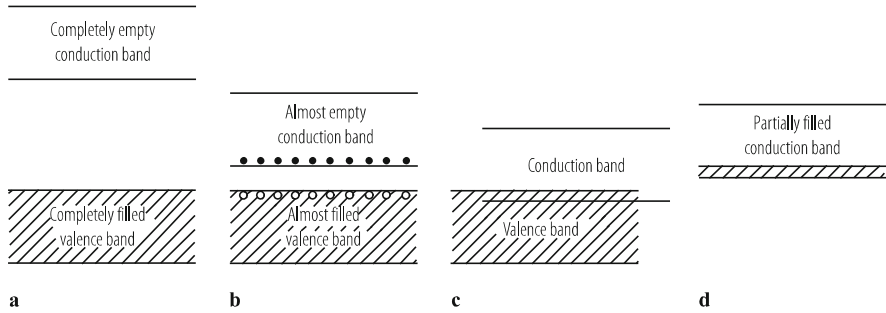
Fig. 5.2 Energy band structure of insulators (**a**), semiconductors (**b**), and conductors (**c, d**)

from the conduction or valence band, respectively. silicon doped with donor atoms is called *n*-type, and *p*-type for acceptors. These states are already ionized well below room temperature, and the electrons or holes can move freely in the silicon lattice, resulting in a decrease of the resistivity. For silicon detectors crystals with a typical doping density of 10^{12} cm^{-3} are used, which results in a similar density of free charge carriers and a significantly reduced resistivity of a few kΩ·cm. Applying an external electric field the free charge carriers can be removed and a space charge region due to the surplus charge of the doping atoms is created.

The discussion so far has used the simple bond picture. A more sophisticated treatment that allows also quantitative calculations requires the quantum mechanical band model. While single atoms possess discrete energy levels, in crystals these are transformed into energy bands.

Figure 5.2 shows the (almost) fully occupied valence band and the lowest laying (almost) empty conduction band for insulators, semiconductors and conductors. In insulators (a) valence and conduction band are separated by a big band gap so that electrons cannot be thermally excited from the valence to the conduction band. Conductors have overlapping bands (c) or a partially filled conduction band (d) and are therefore electrically conducting.

In intrinsic (undoped) semiconductors only a small fraction of the electrons in the valence band are thermally excited into the conduction band. Extrinsic (doped) semiconductors have additional localized energy states within the band-gap. Donor states close to the conduction band (e.g. P in Si) emit their electrons into the conduction band and are (almost) completely ionized (positively charged) already well below room temperature. Acceptor states close to the valence band trap electrons and leave holes in the valence band.

In thermal equilibrium the occupation probability F of states with energy E at temperature T follows from Fermi statistics

$$F(E) = 1/\left(1 + \exp\left(E - E_{\mathrm{f}}\right)/kT\right), \qquad (5.1)$$

with k the Boltzmann constant. The overall charge neutrality determines the Fermi level E_{f}.

Electrons bound in one of the localized donor states may be emitted into the conduction band by thermal excitation with a probability ε_n, thereby ionizing donors. Ionized donors may also capture electrons out of the conduction band. This process is described by a capture cross section σ_n. In thermal equilibrium these two processes have to balance each other. That condition allows to derive a relation between emission probability ε_n and capture cross section σ_n:

$$\varepsilon_n = \sigma_n \, v_{th\,n} \, n_i \, \exp\left((E_d - E_i)/kT\right), \tag{5.2}$$

with $v_{th\,n}$ thermal velocity of electrons in the conduction band, n_i intrinsic carrier concentration, E_d donor energy level, E_i intrinsic energy (Fermi level for an intrinsic semiconductor). This relation is valid more generally and can be applied to non-equilibrium conditions.

Electrons in the conduction band and holes in the valence band can move freely within the crystal lattice, their movement being only retarded by scattering on imperfections of the lattice. These imperfections may be due to lattice defects, doping atoms replacing regular atoms of the crystal (substitutional dopands) and distortions of the lattice due to thermal vibrations. The simplified way of describing these effects uses the assumption that charge carriers are accelerated by the electric field and lose all previous history at each scattering, starting with random thermal velocity again.

The movement due to the electric field is described by the drift velocity that for low fields can be assumed to be proportional to the electric field:

$$v_n = \left(-q\tau_c/m_n\right) E = -\mu_n \, E, \qquad v_p = \left(q\tau_c/m_p\right) E = \mu_p \, E, \tag{5.3}$$

with v_n, v_p, μ_n, μ_p being the drift velocities and low-field mobilities of electrons and holes, respectively, q elementary charge, τ_c average time between collisions, m_n, m_p effective masses of electrons and holes, and E electric field. For a high electric fields τ_c decreases and the drift velocity saturates.

At very high electric field electrons and holes may acquire sufficient energy in between collisions to generate additional electron hole pairs. This avalanche process can be the cause for an electrical breakdown of devices. It may also be used as an intrinsic amplification process in order to get sufficiently high signals from very small ionization.

For inhomogeneous carrier distributions charge carriers will preferably diffuse from high concentrations to regions of lower concentrations. This diffusion mechanism is described by

$$F_n = -D_n \, \nabla n, \qquad F_p = -D_p \, \nabla p. \tag{5.4}$$

With F_n, F_p flux of electrons and holes, D_n, D_p diffusion constant. Electron and hole current densities due to drift and diffusions are given by

$$J_n = -q\mu_n \, nE + qD_n \, \nabla n, \qquad J_p = q\mu_p \, pE - qD_p \, \nabla p. \tag{5.5}$$

Diffusion constant and mobility are related by Einstein's relation $D = (kT/q)\,\mu$. It can be derived from the requirement of zero current in thermal equilibrium of a device with non-uniform doping that has to have a constant Fermi level.

In the absence of magnetic fields charge carriers will move approximately parallel (holes) or antiparallel (electrons) to the electric field. The magnetic field adds a force perpendicular to the direction of motion and to the magnetic field direction so that the charge carriers move at an angle $\theta_p = \mu^H_p \, B$, $\theta_n = \mu^H_n \, B$ with respect to the drift direction. The Hall mobilities μ^H_p and μ^H_n differ from the drift mobilities μ_p and μ_n. B is the magnetic field component perpendicular to the electric field and the particle velocity.

5.4 Radiation Damage

Damage by ionizing and non-ionizing radiation, represents a major limitation for the use of silicon detectors in the harsh radiation environment of high-luminosity colliders, like the CERN LHC, where after its upgrade, fluences exceeding 10^{16} cm^{-2} and dose values up to 5 MGy will be reached. At high-brilliance X-ray sources, like the European X-ray Free-Electron Laser at Hamburg, dose values up to 1 GGy are expected. Radiation damage is classified in surface and bulk damage.

Surface damage is caused by ionization by charged particles and X-ray photons in the insulating layers, e.g. the SiO_2, required to fabricate silicon sensors. Like in the silicon bulk, ionizing radiation produces electron-hole pairs in the SiO_2. Whereas the mobility of electrons is sufficiently high so that they can move to a nearby electrode, holes are trapped, which results in a positive charge layer and interface traps at the Si-SiO$_2$ interface [4]. Positive surface charges can result in an electron accumulation layer in the Si at the interface, which can cause shorts between electrodes or break down. Interface traps, if exposed to an electric field, produce surface-generation currents. As the exact conditions at the Si-SiO$_2$ interface also depend on the potential on the outer SiO_2 surface, which in particular in dry conditions has a very high surface resistance (sheet resistance $> 10^{18}$ $\Omega_\square$), it can take days until equilibrium is reached [5]. The result can be a breakdown after several days of operation or a humidity-dependent breakdown voltage. Surface radiation damage also depends on the dose-rate, which together with long time constants has to be taken into account, when studying surface damage or when testing silicon detectors. Surface damage is also technology dependent. In addition, already at room temperature significant annealing takes place. All these effects make a systematic study of surface-radiation damage difficult and time consuming. However, also thanks to the methods developed for radiation-hard electronics,

surface-radiation effects are sufficiently well understood and can be avoided by a proper design [6]. Nevertheless, there are many examples of improper designs and several unpleasant surprises due to surface damage.

Non-ionizing interactions, which knock out silicon atoms from their lattice points, are the main cause of bulk damage. A minimum energy transfer to the silicon atom of about 25 eV is required to produce such a primary defect. For energy transfers above 1 keV the silicon atom itself can knock out further silicon atoms, resulting in defect clusters, and for energies above 12 keV multiple clusters can be produced. These threshold numbers are the result of model calculations and only limited experimental information is available. The primary defects are mobile at room temperature. Some of them anneal, others diffuse to the silicon surface or interact with crystal defects and impurities and form stable defects. Using different spectroscopic methods a large number of defects could be identified and their properties, like donor- or acceptor-type, position in the band gap, cross-sections for electrons and holes and introduction rates determined [7]. The electrically active defects have three main consequences for detectors: (1) Increase of dark current, (2) trapping of signal charges thus reducing the charge collection, and (3) change of the electric field in the space charge region from which the signal charge is collected.

Typical introduction rates of stable defects are of order 1 cm^{-1}, i.e. a fluence if 1 particle per cm^2, produces 1 stable defect per cm^3. For fluences above about 10^{14} cm^{-2}, the density of defects exceeds by far the doping density, and the silicon properties change significantly: In non-depleted silicon the high generation-recombination rate results in an approximately equal density of holes and electrons, and the resistivity increases from the value determined by the dopant density to the value of intrinsic silicon, which is about 350 kΩ·cm at room temperature. The high dark current for a reverse biased diode, which is dominated by holes at the cathode and by electrons at the anode, results in a position-dependent filling of the defects and a completely different electric field distribution than in the detector before irradiation. High field regions appear at anodes and cathodes, a phenomenon called "double junction", and lower field regions in-between [8, 9]. Thus the concept of uniform doping breaks down and most of the methods used to characterize silicon before irradiation are no more applicable.

Based on a detailed and systematic study of silicon pad diodes with different doping and impurities irradiated by different particles and fluences, the phenomenological *Hamburg model* has been developed [10]. It parametrises the change of parameters like dark current and effective doping, used to characterise non-irradiated sensors, as a function of irradiation fluence and temperature history. Up to fluences of approximately 10^{14} cm^{-2}, which are presently (mid 2018) reached at the LHC, the model is remarkable successful in describing the observed effects of radiation damage. An extension of such a model to higher fluences is badly needed for monitoring the radiation fields at the LHC and for the planning of the experiments at the High-Luminosity LHC.

5.5   Semiconductor Detector Principles

The very basic and most common detector type, the reverse-biased diode, has already been sketched in Sect. 5.2. Here we will give some more information on this device and also present some more sophisticated principles, the semiconductor drift chamber and the DEPFET detector-amplification structure, while detectors based on the avalanche mechanism will be discussed in a later chapter.

5.5.1   Reverse Biased Diode (as Used in Strip and 3-D Detectors)

The principle of a reverse biased diode has already been sketched in Sect. 5.2. Here a more detailed discussion is given. Even without applying a bias the *p-n* junction develops a space charge region due to the diffusion of electrons and holes across the junction leading to a surplus of negative charge on the *p*-side and of positive charge on the *n*-side of the junction. This creates an electric field, a drift current and a space charge region on both sides of the junction. At any point of the device drift and diffusion currents cancel each other in equilibrium without external bias. Such a device can already be used as radiation detector since electron–hole pairs created in the space charge region will be separated by the electric field thus create a current across the junction.

Reverse biasing will increase the space charge region and therefore the electric field. For a strongly asymmetric, but in each region uniformly doped p^+n junction (as shown in Fig. 5.1) the depth of the space charge and therefore the sensitive region increases with the square root of the applied voltage.

Reverse biased diodes have been used as energy sensitive radiation detectors in Nuclear Physics for quite some time. The real breakthrough came with strip detectors in Particle Physics used for particle tracking with micro-meter accuracy. Many small strip-like diodes were integrated on the same wafer and each one connected to its own readout channel (Fig. 5.3). The particle position was given by the channel giving the signal. More sophisticated strip detectors will be described in Sect. 5.6.

Planar pixel detectors are obtained by shortening the individual strips so that they do not reach anymore the detector edge and form a two-dimensional pattern. Detectors with pixel sizes down to $15 \times 15\,\mu m^2$ have been built. The main difficulty of such detectors is their readout. Different realisations will be discussed later.

A different concept of diode detectors, the so called 3-D detectors [11], is shown in Fig. 5.4: Holes with diameters of a few micro-meters are etched into the crystal orthogonal to its surface, and alternate holes are n^+- and p^+-doped. A voltage difference between the n^+- and p^+-doped columns generates an electric field parallel to the crystal surface. The number of electron-hole pairs produced by a charged particle traversing the detector at large angles to the surface is given by
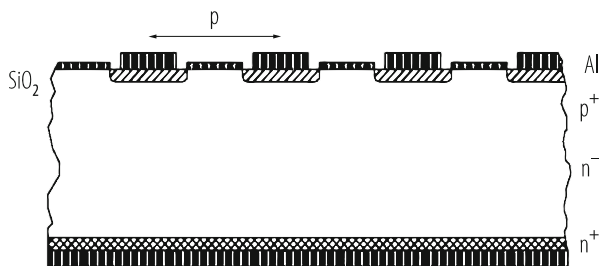
Fig. 5.3 Cross section of a silicon strip detector built on lightly phosphor doped (n^-) silicon bulk material. Strips are highly boron doped (p^+) and the backside highly phosphor doped (n^+)
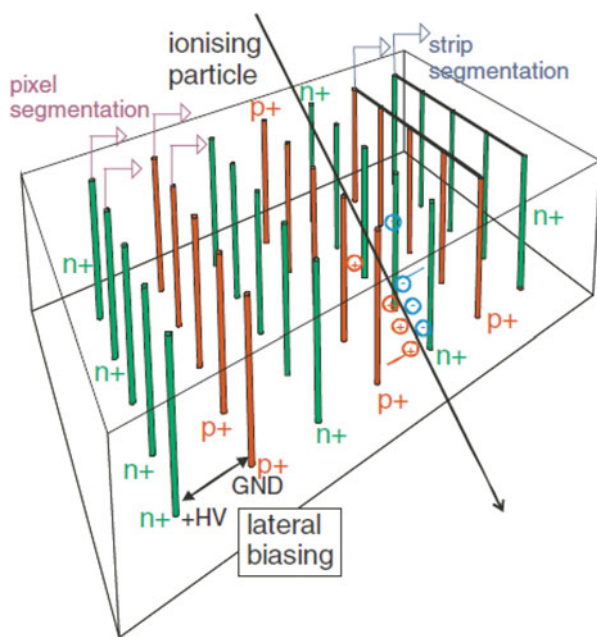
Fig. 5.4 Principle of the 3-D detector: Holes are etched into the silicon crystal orthogonal to the detector surface. Alternate holes are n^+- and p^+-doped. A positive voltage on the n^+-contacts, with the p^+-contacts grounded, generates an electric field parallel to the detector surface. In a 3-D detector the charge generated, given by the crystal thickness, and the charge collection distance, given by the distance between the holes, can be separately chosen (Book F. Hartmann Fig. 1.69)

the crystal thickness, whereas the charge collection distance is given by the column distance. In this way signal and charge collection distances can be chosen separately and the detector can be optimised for radiation tolerance. In addition, the operating voltage for 3D-detectors and thus the power heating the detector are significantly reduced compared to planar detectors. By connecting the p^+- and n^+-columns with

different metal patterns, strip- and pixel-sensors and other readout geometries can be realized.

5.5.2 Semiconductor Drift Chamber

The semiconductor drift chamber has been invented by Emilio Gatti and Pavel Rehak [1]. This device (Fig. 5.5) makes use of the sideward depletion principle, having diode junctions on both surfaces and a bulk contact on the fringe. Fully depleting the device by applying a reverse bias voltage between p- and n-contacts creates a potential valley for electrons in the middle plane. Electrons created by ionizing radiation will assemble in this valley and subsequently diffuse until they eventually reach the n-doped anode. Faster and controlled collection is achieved by adding a horizontal drift field. This is obtained by dividing the diodes into strips and applying from strip to strip increasing voltages.

   This device is able to measure position (by means of the time difference between particle interaction and arrival of the signal at the anode) as well as the energy from the amount of signal charge. In many applications the latter aspect is the important one. Here one profits from the small electric capacitance of the anode compared to the planar diode shown in Fig. 5.1, which acts as capacitive load to the readout amplifier. Large area detectors can therefore be operated with excellent energy resolution at high rates.
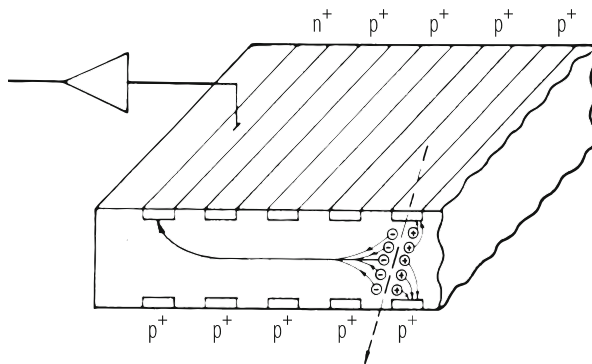
Fig. 5.5 Semiconductor drift chamber using the sideward depletion method. Dividing the p^+ doped diodes into strips and applying a potential which increases from strip to strip superimposes a horizontal field in the potential valley that drives the electrons towards the n^+ anode which is connected to the readout electronics. Upon arrival of the signal charge at the n^+ anode the amount of charge and the arrival time can be measured
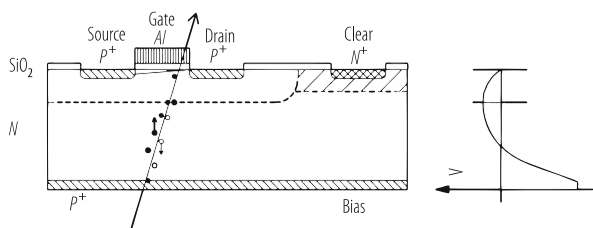
Fig. 5.6 The concept of a DEPFET: Simplified device structure (*left*) and potential distribution along a cut across the wafer in the gate region of the transistor (*right*)

5.5.3 DEPFET Detector-Amplification Structure

The *DEPFET* structure which simultaneously possesses detector and amplification properties has been proposed by J. Kemmer and G. Lutz in 1987 [3] and has subsequently been confirmed experimentally [12]. It is based on the combination of the sideward depletion method—as used in a semiconductor drift chamber shown in Fig. 5.5—and the field effect transistor principle.

In Fig. 5.6 a *p*-channel transistor is located on a fully depleted *n*-type bulk. Compared to Fig. 5.5 the potential valley has been moved close to the top side. Signal electrons generated in the fully depleted bulk assemble in a potential minimum for electrons ("internal gate") and increase the transistor channel conductivity in a similar way as by changing the (external) gate voltage. The device can be reset by applying a large positive voltage on the clear electrode.

The DEPFET has several interesting properties:

- Combined function of sensor and amplifier;
- Full sensitivity over the complete wafer;
- Low capacitance and low noise;
- Non-destructive repeated readout;
- Complete clearing of the signal charge: No reset noise.

These properties make it an ideal building block for an X-ray pixel detector, or for a pixel detector for the precision tracking of charged particles.

5.6 Silicon Strip Detectors (Used in Tracking)

Silicon strip and pixel detectors are the most common semiconductor detectors in Particle Physics, mostly used for particle tracking. There one profits from the precise position measurement (few μm) at very data rates (up to tenths of MHz per detection element). In its simplest form they are narrow strip diodes put next to each other on the same semiconductor substrate, each strip having its own readout channel. Typical charge collection times are about 10 ns. Due to diffusion, track

inclination and the Lorenz force in a magnetic field, the charge of one track may be distributed over two or more strips. This can be exploited to improve the accuracy of the position measurement well below the value given by the strip pitch. It is then limited by fluctuations of the ionization process and in particular the generation of delta electrons and the electronics noise. A measurement precision down to about 1 μm has been achieved.

5.6.1 Strip Detector Readout

In the conceptually simplest version each strip is connected to its own electronic readout channel and the position is determined by the number of the strip providing a signal.

Binary (yes/no) *readout* may be used if no energy information is required and if the position accuracy given by the strip pitch is sufficient. One also does not lose position resolution compared with analogue readout if the strip pitch is large with respect to the width of the diffusion cloud.

Analogue (signal amplitude) *readout* of every channel may lead to a substantial improvement of the position measurement precision if the strip spacing matches the charge spread due to diffusion during collection. (Charge spread can also be due to track inclination or the Lorenz angle in a magnetic field.) In addition, the simultaneous measurement of energy loss becomes possible.

Charge division readout reduces the number of readout channels as only a fraction of the strips is connected to a readout amplifier (Fig. 5.7). Charge collected at the other (interpolation) strips is divided between the two neighbouring readout channels according to the relative position. Charge division is due to the capacitors between neighbouring strips. For charge division to work, it is necessary to hold the intermediate strips at the same potential as the readout strips. This can be accomplished by adding high ohmic resistors or with other methods. If the intermediate strips were left floating, they would adjust themselves to a potential
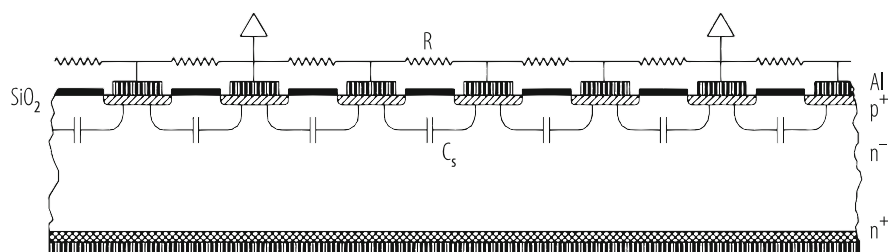
Fig. 5.7 Charge division readout. The interstrip capacitors between the readout strips act as capacitive charge divider. The high-ohmic resistors are required to keep all strips at the same potential

such that they would collect no signal charge, and thus charge division would cease to function.

5.6.2 Strip Detectors with Double-Sided Readout

As shown in Fig. 5.8 it is possible to segment the electrodes on both sides of the wafer. This double-sided readout has the obvious advantage of providing twice the information for the same amount of scattering material. With crossed strips on the two detector faces, a projective two-dimensional measurement is obtained from a single detector.

For a traversing particle, a spatial point can be reconstructed as both projections are obtained from the same initial charge cloud. With analogue readout it is furthermore possible (to some degree) to correlate signals from the two sides, making use of Landau fluctuations and the equality of the charge induced on both sides for each ionizing particle. This can be of interest for resolving ambiguities when several particles traverse simultaneously the detector.

A problem in producing double-sided detectors is the insulation of neighbouring strips on both detector sides. The naive solution of only providing highly doped n- and p-doped strips on the two sides of the detector (Fig. 5.8) fails because of the build-up of an electron-accumulation layer (an inversion layer on p-type silicon) between the n-strips below the insulating SiO_2 (Fig. 5.9a). This electron layer results in an electrical shortening of neighbouring strips. It is caused by the positive charges that are always present at the silicon-oxide interface. As discussed in Sect. 5.4 ionizing radiation results in a further increase of positive charges.

There are three possibilities for curing the problem:

1. Large-area p-type surface doping. In this case the oxide charges are compensated by the negative acceptor ions and the build-up of the electron layer is prevented (Fig. 5.9b). This method requires a delicate choice of p-type doping concentration and profile. A too large doping results in high electric fields and in a possible
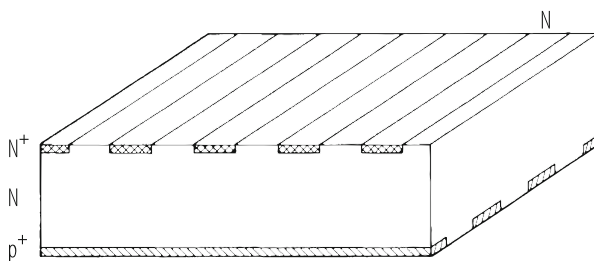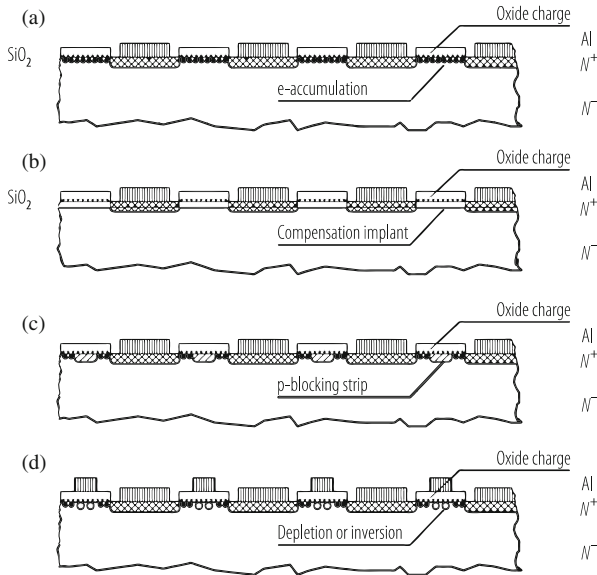

Fig. 5.8 Double sided strip detector (naive solution)

Fig. 5.9 Insulation problem for *n*-strips in silicon, due to electrical shortening by an electron accumulation layer (**a**), and three possible solutions: Large area *p*-implantation (**b**); interleaved *p*-strips (**c**) and negatively biased MOS structures (**d**)

electrical breakdown at the strip edges. This problem is alleviated by the other two solutions presented below.

2. Disruption of the electron layer by implantation of *p*-strips between the *n*-doped charge-collection strips (Fig. 5.9c); and

3. Disruption of the electron layer by a suitably biased (negatively with respect to the *n*-strips) MOS structure (Fig. 5.9d). For moderate biasing neither electrons nor holes will accumulate underneath the MOS structure, while for a high negative bias a hole layer (inversion on *n*-type, accumulation on *p*-type silicon) will form.

5.6.3   Strip Detectors with Integrated Capacitive Readout Coupling and Strip Biasing

Capacitive-coupled (AC) readout (Fig. 5.10, *right*) has the obvious advantage of shielding the electronics from dark current, whereas direct coupling (DC, Fig. 5.10, *left*) can lead to pedestal shifts, a reduction of the dynamic range, drive the electronics into saturation or requires a dark-current compensation.

As it is difficult to fabricate high-ohmic resistors, and almost impossible to produce sufficiently large capacitors in LSI electronics, it seemed natural to integrate
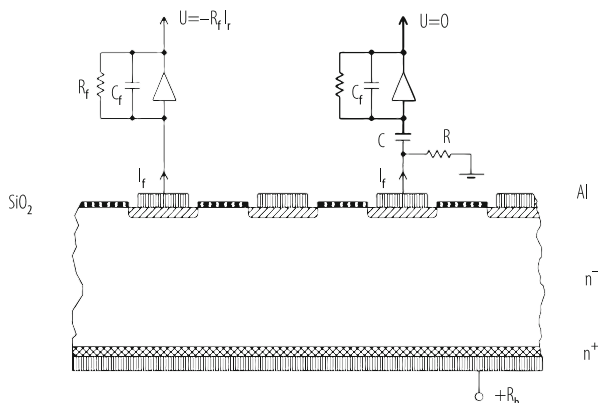
Fig. 5.10 Direct and capacitive coupling of electronics to the detector. With direct coupling (*left*) the detector reverse bias current I_f has to be absorbed by the electronics. With capacitive coupling (*right*), only the AC part of the detector current reaches the electronics, while the DC part flows through the resistor R
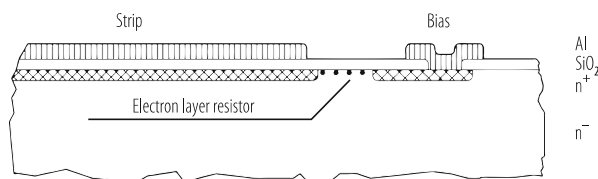

Fig. 5.11 *n*-strip biasing by an electron-accumulation-layer resistor. The diagram shows a cut along the strip direction. The electron layer is induced by the always present positive oxide charges that attract electrons towards the Si-SiO$_2$ interface. It is sidewise enclosed by p-implants so as to prevent electrical shortening between neighbouring strips. Bias and strip implants are at nearly the same potential

these elements into the detector. This has been done in a collaborative effort by a CERN group with the Center of Industrial Research in Oslo [13], where the detectors were produced. Capacitances have been built by separating implantation and metallization of the strips by a thin SiO$_2$ layer. Biasing resistors were made of lightly doped polysilicon, a technology that is used in microelectronics. The detectors gave very satisfactory results. The strip detectors of several particle physics experiments use this design.

A different method of supplying the bias voltage to the detector has been developed and used for double-sided readout by a Munich group [3, 12]. It leads to a considerable simplification of the technology as it does not require resistors but only uses technological steps that are already required for DC coupled detectors. The polysilicon technology can be avoided altogether; instead, the voltage is supplied through the silicon bulk. Two methods can be applied either using the resistance of an electron accumulation layer (Fig. 5.11) that is induced by the positive oxide charge or a punch through mechanism that occurs between two closely spaced *p*-
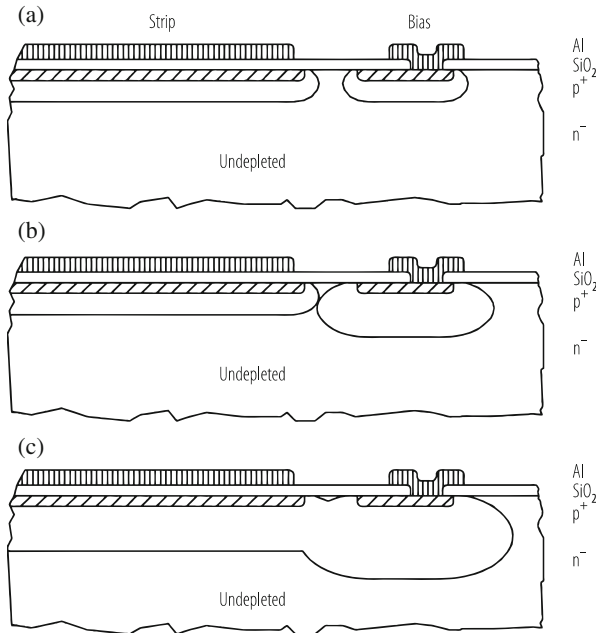
Fig. 5.12 *p*-strip punch-through biasing. The diagrams show cuts along the strip direction: (**a**) Before applying a bias voltage, where the space-charge regions around the strip and the bias implant are isolated; (**b**) at onset of punch-through, where the space-charge region around the bias implant has grown and just touches the space-charge region of the strip. The potential barrier between strip and bias implants has diminished, but is just large enough to prevent the thermal emission of holes towards the bias strip; (**c**) at larger bias voltage, where the space-charge region has grown deeper into the bulk. Holes generated in the space-charge region and collected at the strip implant are thermally emitted towards the bias strip. The voltage difference between strip implant and bias depends on geometry, doping and bias voltage. A weak dependence on oxide charge is also present

electrodes (Fig. 5.12). These biasing methods can be used for single sided and also for double sided readout where *p*- and *n*-strips are located at opposite surfaces of the wafer as was the case in the ALEPH experiment. In all cases the capacitors are built by interleaving a thin oxide layer between implantation and metal strips.

A word of caution on the operation of capacitive-coupled detectors and in particular of double sided detectors will be given at this point since it has been overlooked in a couple of experiments causing detector breakdown. At first glance it seems that one can choose the voltages on implant and metal strips independently. However this can result in shortening of neighbouring strips or electrical breakdown due to the build-up of accumulation layers at the Si-SiO$_2$ interface. Although the SiO$_2$ is not covered with an ohmic layer its surface will slowly charge up to a potential close to the neighbouring metal electrodes, because of a high but finite surface resistivity, as discussed in Sect. 5.4.

5.7   Detector Front-End Electronics

Before discussing more sophisticated detectors we now turn to readout electronics, a subject relevant to all detectors. As there is a close interplay between a detector and its electronics, both components have to be considered together when designing a detector for a specific application. In most cases a signal charge produced by photons or ionizing radiation has to be measured as precisely as possible in a predefined time interval and with tolerable power consumption. Readout uses in most cases large scale integrated (LSI) electronics adapted to the needs of the special application.

5.7.1   Operating Principles of Transistors

Transistors are commonly classified into unipolar and bipolar, depending on whether only one or both types of charge carriers participate in the current flow. As a consequence of the difference in operating principles, their properties—and therefore their suitability for specific applications—differ greatly. Bipolar transistors are well suited for high-speed applications and for driving large currents. Unipolar transistors are common in moderate-speed low-noise applications (JFETs) and are most prominent in digital circuitry (MOSFETs).

We use as an example the n-channel MOSFET (Metal-Oxide-Semiconductor Field Effect Transistor). Figure 5.13 shows a cross section along the channel. Two n^+p diodes are connected by a MOS structure. Applying a high enough positive potential on the gate an inversion (electron) layer will connect source and drain and for non-zero drain-source voltage an electron current will flow from source to drain. The strength of this current can be controlled by the gate potential and also

Fig. 5.13 n-channel MOSFET: Cross-section (**a**) and device symbol (**b**). The separation of the space-charge region from the channel below the gate and from the undepleted bulk is indicated by the dashed lines
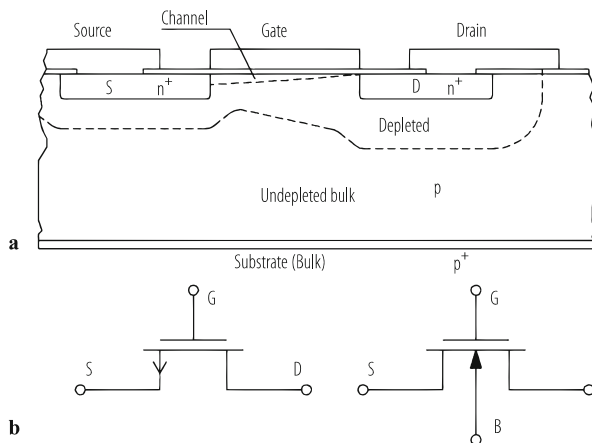
by the drain voltage. A resistive voltage drop along the channel is responsible for the current saturation that occurs once this voltage drop equals the effective gate voltage (voltage above the threshold necessary to create inversion).

Important parameters of the transistor to be used in noise considerations are the transistor (output) conductance $g = dI_d/dV_d$ and transconductance $g_m = dI_d/dV_g$. These and other parameters can be modelled using the graded channel approximation which relies on the assumption that changes along the channel are much smaller than those occurring in the transverse direction. It allows deriving scaling laws for changes in geometry. However, for microelectronics with minimal feature size these are of limited validity. Instead, two- and three-dimensional numerical device simulations are needed.

Measurement precision is limited by noise. There are several noise mechanisms present. Considering a resistor with resistance R for example, the thermal motion of electrons will result in a statistical fluctuation of the charge distribution in the conductor, leading to a noise voltage density of $d<v_n^2>/df = 4\,kT{\cdot}R$ between the terminals of the resistor. The resistance of the MOSFET channel is a source of white noise too. It is customary to represent this noise by a voltage at the gate $d<v_n^2>/df = 4\,kT(2/3)(1/g_m)$ for the operation of the transistor in the saturation region.

A further mechanism of noise is the capture and delayed release of single charge carriers in the channel. While being captured the drain current decreases, returning to the initial value when released. For a single trapping centre with characteristic average capture and release times a Lorentzian noise spectrum as function of frequency results. Having many different trapping centres, as is the case for traps at the Si-SiO$_2$ interface where trapping and detrapping occurs by means of tunnelling, the result of the superposition of Lorentzian noise spectra is a $1/f$ spectrum $dv_n^2/df = A_f/f$ with A_f a constant, which depends on the technology and the geometric parameters of the transistor. A_f is usually obtained from measurements and parameterized as $A_f = K_F/(WLC_{ox}^2)$. K_F characterizes the technology, W and L are channel width and length, and C_{ox} the oxide capacitance per unit area. Note that the *1/f* noise is independent of the transistor current.

5.7.2   The Measurement of Charge

The standard problem in the readout of a semiconductor detector is the low-noise measurement of the signal charge, usually under severe constraints such as high-speed operation, low power consumption, restricted space and frequently high radiation levels. In this section the general problems of charge measurement will be addressed, while specific solutions for the electronics will be considered later.

The *charge-sensitive amplifier* (CSA), invented by Emilio Gatti [14] and represented in Fig. 5.14, consists of an inverting amplifying circuit which—in the ideal case—delivers an output voltage proportional to the input ($U_{out} = -A\,U_{in}$) and a feedback capacitor C_f. In addition, a high-resistance feedback or a switch is needed in the feedback loop, in order to bring the circuit into its operating condition. C_D
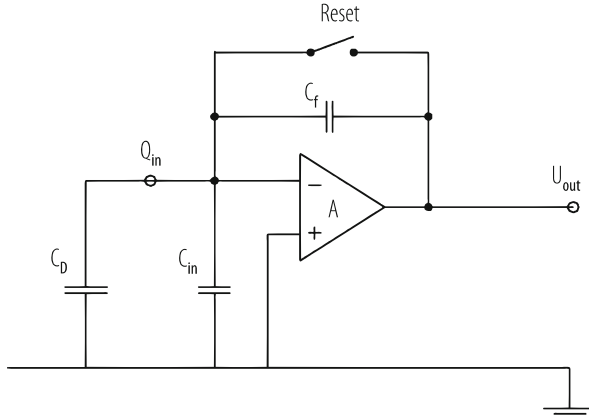
Fig. 5.14 Principle of a Charge Sensitive Amplifier (CSA). The inverting amplifier has gain A and a capacitive feedback. The reset switch is only used for bringing the system into its operating condition, and is often replaced by a high-ohmic resistor

represents the capacitive load of the detector at the input, C_{in} the capacitive load to ground in the amplifier, which is usually dominated by the gate capacitance of the input transistor.

Putting a charge Q_{in} at the input will result in an output voltage change of $U_{out} = -Q_{in}/(C_f +(C_D+C_{in}+C_f)/A)$ which for large amplification is given by the ratio of signal charge over feed-back capacitance, indicating that the charge has been transferred completely from the detector to the feedback capacitor. For low frequencies the input impedance of the CSA will be represented by a capacitance of the value $C_{eff} = (A+1) C_f + C_{in}$. A high value of $C_{eff} > C_D$, i.e. a low input impedance, is important because when C_{eff} is only of the same order of magnitude as the detector capacitance C_D the charge is incompletely transferred to the electronics. This results in a loss of sensitivity and possibly crosstalk within the detector to neighbouring channels.

Turning now to the question of measurement precision, respectively noise in the detector-amplifier system, we remark that it is customary to represent the effect of all amplifier noise sources by a single noise voltage U_n placed at the input (Fig. 5.15). As this noise voltage generator is in series with detector and amplifier it is called serial noise. The presence of the serial noise voltage U_n will result in an output voltage even if there is no signal charge present. For an evaluation of the serial noise charge, it is easiest to consider the charge necessary to compensate for the effect of the noise voltage, such that the output voltage remains at zero. The value can be immediately read from Fig. 5.15: $Q_n = U_n (C_D + C_{in} + C_f) = C_T U_n$ with C_T the total "cold" input capacitance.

Notice that the serial noise is generated in the amplifier, the influence of the detector is due to the capacitive load at the amplifier input only. The detector itself produces noise due to statistical fluctuations of its leakage current I. This parallel
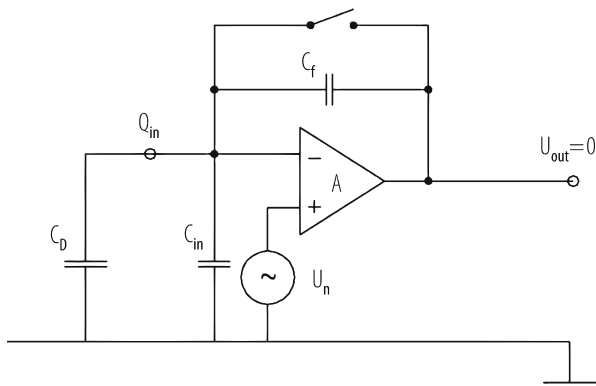
**Fig. 5.15** The effect of amplifier serial noise in a detector-amplifier system

noise is represented by a noise current source of density $d<i_n^2>/df = 2I \cdot q$ in parallel to the detector capacitance C_D. To estimate the charge measuring precision one has to follow separately signal and noise through the complete readout chain and compare their respective output signals.

The signal produced by the amplifier will usually not be used directly; it will be further amplified and shaped, in order to optimize the ratio of signal to noise and to reduce the interference between subsequent signals. We will only consider a few very simple cases, the simplest being an idealized charge-sensitive amplifier followed by an RCCR filter. For a more elaborate treatment, the reader is referred to the literature (e.g. [15]).

The arrangement of a CSA followed by an RCCR filter is shown in Fig. 5.16. The output of the CSA is a voltage step given for very high amplification as Q/C_f. The shaper does an RC integration followed by a CR differentiation. This procedure results in a signal peak, which for the same integration and differentiation time constant $\tau = R_1 C_1 = R_2 C_2$ has the shape $U_{out}(t) = (Q/C_f) \cdot (t/\tau) \cdot \exp(-t/\tau)$ with a peak value $U_{peak} = (Q/C_f) \cdot \exp(-1)$. The height of this peak is a measure of the signal charge. Superimposed on the signal is the noise voltage, and we are interested in the signal-to-noise ratio, which is defined as the ratio of the height of the peak value to the root-mean-square value of the noise voltage measured at the same point in the circuit.

In order to find the noise voltage at the output, each noise source in the circuit has to be traced to the output and the resulting voltages added in quadrature. Doing so, one finds the important result that, for white (thermal) serial noise, the ratio of noise to signal (N/S) decreases with the square root of the shaping time constant τ, while for *1/f* noise this ratio remains constant. Parallel noise, given as a time integral over current fluctuations, increases with the square root of the shaping time.

More sophisticated continuous time filtering methods use (for example) Gaussian shape filtering, which can be approximated by several sequential RC integration and differentiation steps. Especially important in integrated electronics are the
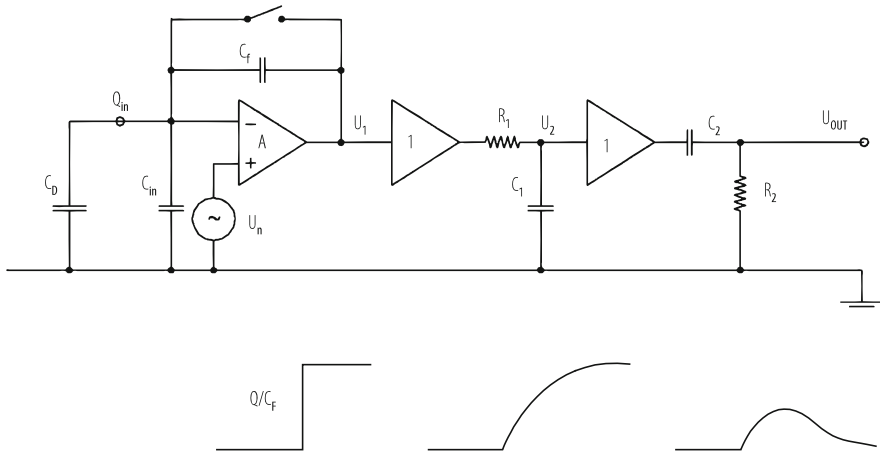
Fig. 5.16 Noise filtering and signal shaping in an RCCR filter following a charge-sensitive amplifier (top). The two unity gain amplifiers have been introduced in order to completely decouple the functions of the CSA, the integration (RC) and the differentiation (CR) stages. The signal form is indicated for each stage (bottom)

techniques in which the output signal is sampled several times and mathematical manipulations of the samples are performed. This can be done either after the measurement by numerical processing or directly by the local readout electronics. In the latter case, it is usually achieved by using switched capacitor techniques for analogue algebraic manipulations. Common to both methods, however, is the need to sample the signal at fixed (or, at least, known) times with respect to its generation. Alternatively with frequent enough sampling, the arrival time of the signal can be extracted from the data and filtering can be done afterwards by selecting the relevant samples before and after arrival of the signal. In all cases, however, the fact that the three noise components (white serial, $1/f$ and white parallel noise) scale with the available readout time in the described way remains valid.

As a further example we discuss double correlating sampling realized in switched capacitor technology which is most naturally realizable in integrated circuit technology. It is applicable if the signal arrival time is known in advance, as is the case for example in collider physics experiments.

The circuit (Fig. 5.17) consists of two sequential charge-sensitive amplifiers connected by a coupling capacitor C_s and switch S_c. Initially all switches are closed. Thus both CSAs have reset their input and output voltages to proper working conditions and a possible offset voltage between CSA1 and CSA2 is stored on capacitor C_s. The following operations are performed in sequence: (1) opening switch S_1 at time t_1, resulting in an unwanted charge injection into the input of CSA1 and therefore an output voltage change that will be stored on capacitance C_s and thus made invisible to the input of CSA2; (2) opening of reset switch S_2. Any voltage change on the output of CSA1 (e.g. signal or noise) is also seen in the output of CSA2, amplified by the ratio C_s/C_{f2}; (3) signal charge Q_s generation at time t_3
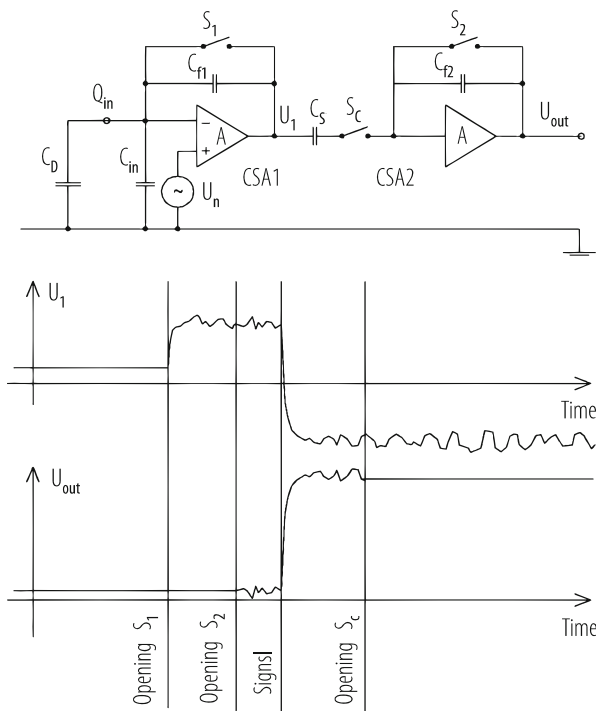
Fig. 5.17 Double-correlated sampling of the output of a charge-sensitive amplifier (CSA1) with the help of a coupling capacitor C_s and a second CSA2

changes the output of CSA1 by $\Delta U_1 = Q_s/C_{f1}$ and the output voltage by $\Delta U_{out} = Q_s (C_s /(C_{f1} C_{f2}))$; and (4) opening of switch S_c at time t_4 inhibits further change of the output voltage. The difference of the output voltage of CSA1 (amplified by C_{f2}/C_s) between times t_2 and t_4 remains present at the output of the circuit.

Double correlated sampling suppresses the reset noise due to operating switch S_1 and also suppresses low frequency noise but enhances the noise at higher frequencies. As a result white noise is not suppressed. This has to be done by limiting the frequency range of the amplifier. More sophisticated schemes of switched capacitor filtering, taking several samples (sometimes with different weights), have also been implemented.

5.7.3 Integrated Circuits for Strip Detectors

The development of integrated detector readout electronics was initiated by the simultaneous requirements of high density, low power and low noise for use with silicon strip detectors in the tight space environment of elementary particle physics
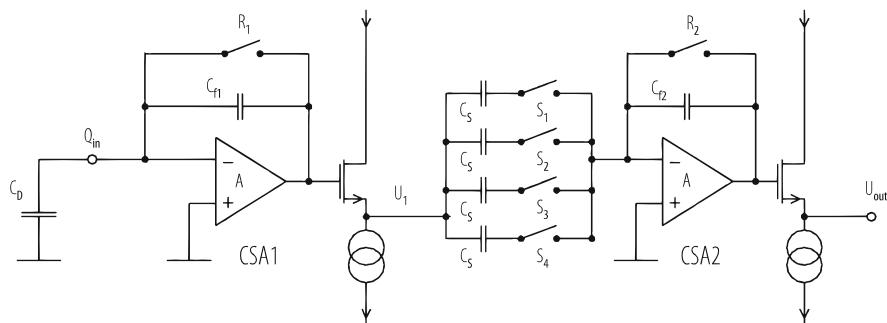
Fig. 5.18 Single channel readout schematics of the CAMEX64 strip-detector readout circuit

collider experiments. A variety of circuits has been developed for this purpose, the basic principle of essentially all of them being: (1) parallel amplification using a charge-sensitive amplifier at each input; (2) parallel signal filtering combined with second-stage amplification and parallel storage within capacitive hold circuits; and (3) serial readout through one single output channel.

We will present only one of the developments [16]. This was not only one of the first to be started but is still in use and has been further developed for many important applications.

The basic functional principle of a single channel is shown in Fig. 5.18. It consists of two charge-sensitive amplifiers, each followed by a source follower, and four sets of capacitors and switches that connect the output of the first amplifier with the input of the second amplifier. The circuit is rather similar to the one shown in Fig. 5.17, but the essential difference is the fourfold multiplication of the capacitive coupling between the amplifiers. In this way it is possible to perform fourfold double-correlated sampling at times that are shifted relative to each other. This procedure provides a good approximation to trapezoidal shaping, which means averaging the output over time intervals before and after signal arrival and taking the difference between the averaged samples.

The switching sequence that performs this function is the following: (1) Close R_1 and R_2. The charges on the feedback capacitances C_{f1} and C_{f2} are cleared. (2) Open R_1: some (unwanted) charge will be injected into the input by the switching procedure, producing an offset in U_1. (3) Close and open in sequence S_1 to S_4. The U_1 offset values at the four times t_1 to t_4 will be stored on the four capacitors C_s. (4) Open switch R_2. A small offset voltage appears at the output. (5) Deposit signal charge Q_{sig} at input. U_1 changes by an amount of $\Delta U_1 = Q_{sig}/C_{f1}$. (6) Close and open S_1 to S_4 in sequence at times t_1 to t_4. A charge $C_s \Delta U_1$ is inserted into the second amplifier at each sample. The total output voltage is $4C_s \Delta U_1/C_{f2} = Q_{sig}4C_s/(C_{f1}C_{f2})$.

The complete chip, containing 64 channels, also comprises additional electronics, as shown in Fig. 5.19. Three test inputs allow injection of a defined charge through test capacitors. Digital steering signals are regenerated by comparators. The
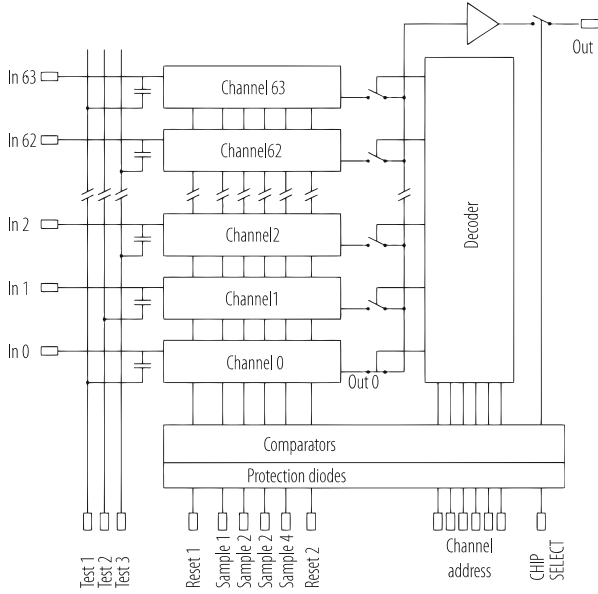
Fig. 5.19 Block diagram of the CAMEX64 strip-detector readout chip
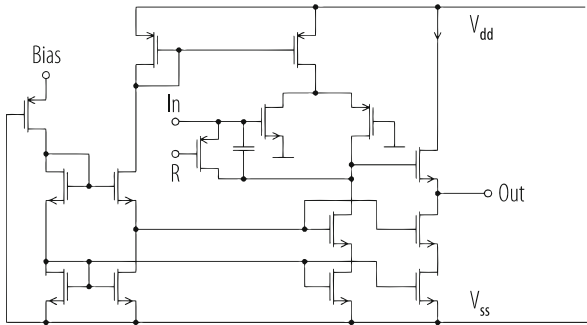
Fig. 5.20 Circuit diagram of the amplifier, including source follower and biasing circuit, of the CAMEX64 strip-detector readout chip

decoder switches one signal at a time on the single output line where a driving circuit for the external load is attached.

A circuit diagram valid for all charge sensitive amplifiers used is shown in Fig. 5.20. The current in all transistors can be scaled by a reference bias current (Bias). The input (In) can be shorted to the output with the reset switch (R) that lies in parallel to the feedback capacitor. The CSA output is connected to a source follower driving the output node (Out).

The circuits mentioned so far have been designed for moderate speed of applications in low-radiation environments. For the CERN Large Hadron Collider

(LHC), where the time difference between consecutive crossings of particle bunches (25 ns) is much shorter than the time it takes to decide whether or not the data of a particular event needs to be kept (approximately 2 μs), chips with high-speed operation and radiation hardness have been developed successfully. In addition to fast low-noise amplifiers and radiation hardness, it is required to store the information for approximately hundred bunch crossings.

The task of designing radiation hard electronics has been considerably eased by the industrial development of submicron integrated circuit technology which, due to the use of ultra-thin oxide, to a large extend has eliminated the problem of radiation induced threshold shifts in MOS transistors [17]. Taking some precautions in the design these technologies can be considered "intrinsically radiation hard".

5.8   Silicon Drift Detectors

The semiconductor drift detector was invented by E. Gatti and P. Rehak [1]. First satisfactorily working devices in silicon were realised in a collaborative effort by J. Kemmer at the Technical University Munich, the Max Planck Institute for Physics in Munich and the inventors [18].

The working principle may be explained by starting from the diode (Figs. 5.1 and 5.21a) if one realizes that the ohmic n^+ contact does not have to extend over the full area of one wafer side but can instead be placed anywhere on the undepleted conducting bulk (Fig. 5.21b). Then there is space to put diodes on both sides of the wafer (Fig. 5.21c). At small voltages applied to the n^+ electrode, there are two space-charge regions separated by the conducting undepleted bulk region (hatched in Fig. 5.21). At sufficiently high voltages (Fig. 5.21d) the two space-charge regions will touch each other and the conductive bulk region will retract towards the vicinity of the n^+ electrode. Thus it is possible to obtain a potential valley for electrons in which thermally or otherwise generated electrons assemble and move by diffusion only, until they eventually reach the n^+ electrode (anode), while holes are drifting rapidly in the electric field towards the p^+ electrodes.

Based on this double-diode structure the concept of the drift detector is realised by adding an additional electric field component parallel to the surface of the wafer in order to provide for a drift of electrons in the valley towards the anode. This can be accomplished by dividing the diodes into strips and applying a graded potential to these strips on both sides of the wafer (Fig. 5.5).

Other drift field configurations (e.g. radial drift) can be obtained by suitable shapes of the electrodes. Drift chambers may be used for position and/or energy measurement of ionizing radiation. In the first case the position is determined from the drift time. Furthermore, segmenting the n^+-strip anode in Fig. 5.5 into pads, a two-dimensional position measurement is achieved.

Due to the small capacitive load of the readout electrode to the readout amplifier, drift detectors are well suited for high precision energy measurement.
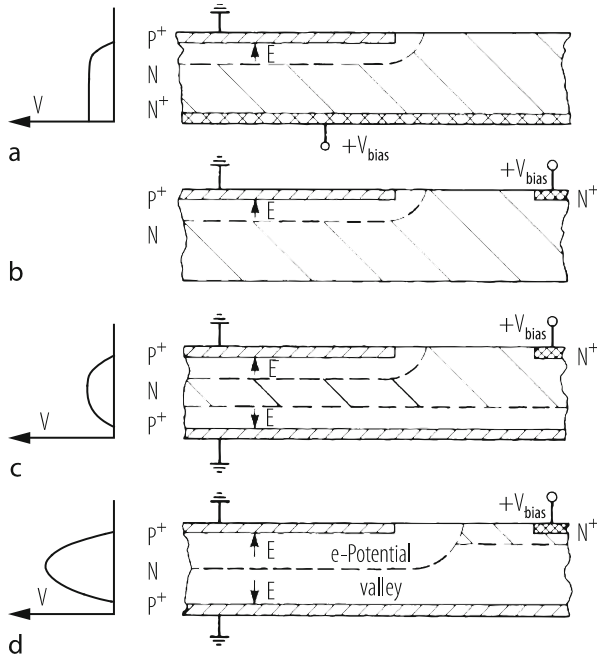
Fig. 5.21 Basic structures leading towards the drift detector: diode partially depleted (**a**); diode with depletion from the side (**b**); double diode partially depleted (**c**); double diode completely depleted (**d**)

5.8.1 Linear Drift Devices

Although linear devices seem to be the most straightforward realisation of the drift detector principle, one encounters some nontrivial problems. They are due to the finite length of the biasing strips and the increasing potential to be applied to these strips, which leads to a very large voltage of several hundred or (for very large drift length) a few thousand volts. Therefore guard structures have to be implemented which provide a controlled transition from the high voltage to the non-depleted region at the edges of the device.

A schematic drawing of the first operational silicon drift detector [18] is shown in Fig. 5.22. Anodes placed on the left and right side of the drift region collect the signal electrons generated by the ionizing radiation. The most negative potential is applied to the field-shaping electrode in the centre. Electrons created to the left (right) of this electrode will drift to the left (right) anode. The p^+-doped field electrodes do not simply end on the side, but some of them are connected to the symmetrical strip on the other half of the detector. In this way one insures that the high negative potential of the field strips drops in a controlled manner towards the potential of the undepleted bulk on the rim of the detector.
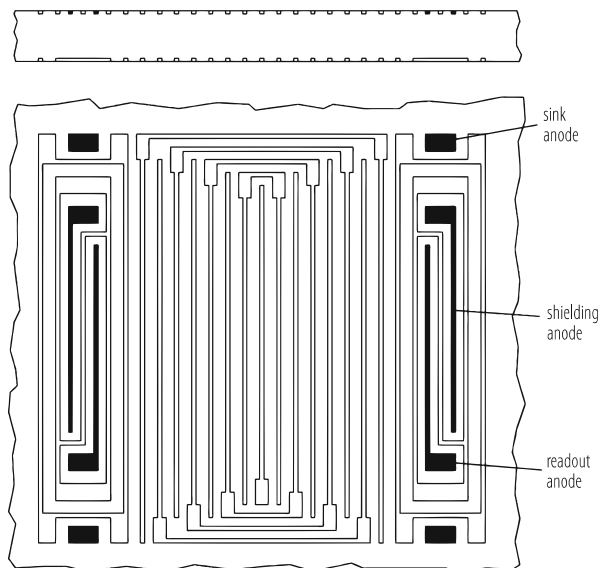
Fig. 5.22 Schematic cross-section and top view of a linear drift detector with *p*-doped field-shaping electrodes (light) and two *n*-doped (double) anodes (dark)

Looking closely at the anodes (Fig. 5.22), it can be seen that there are pairs of *n*-doped strips. Each pair is surrounded by a *p*-doped ring, which also functions as the field-shaping electrode closest to the anode. The two *n*-doped strips are separated by a *p*-doped strip that also connects to the ring surrounding the anode. Surrounding the *n*-strips completely by *p*-doped regions ensures that the adjacent *n*-doped anodes are electrically disconnected to each other and to the other regions of the detector (such as the non-depleted bulk). The outer *n*-strips are used to drain away electrons from the high voltage protection region, while the inner strips measure the signals created in the active detector region.

The opposite side of the silicon wafer is for the large part identically structured. Differences are only in the anode region, where the *n*-implantation is replaced by *p*-doped strips. In the main part of the detector, the strips on opposite sides of the wafers are kept at the same potential, thus assuring a symmetrical parabolic potential distribution across the wafer (Fig. 5.23a). Near the anode an increasing potential difference between the two wafer surfaces moves the potential valley for electrons to the front side until it ends at the anode (Fig. 5.23b).

The linear drift detectors described so far allow one dimensional position measurement only. Dividing the anode of a linear drift detector into pads (Fig. 5.24) leads to a two-dimensional position measurement. One coordinate is obtained from the drift time, the other from the pads on which the signals appear. The second coordinate may be further improved by interpolation using the signal in neighbouring pads. The signal will be distributed over more than one pad if the
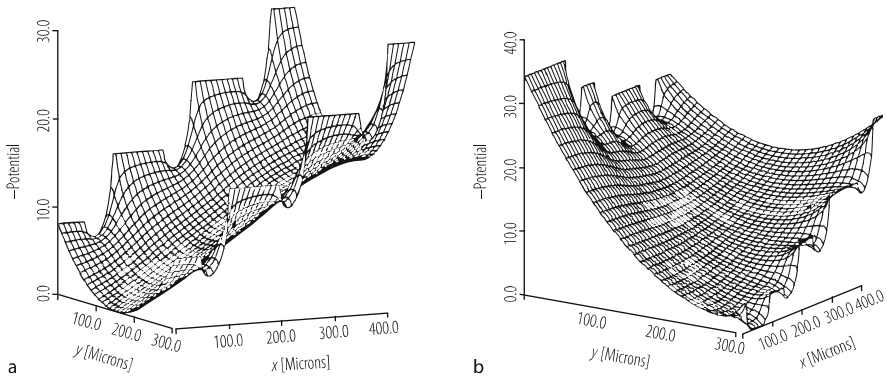
Fig. 5.23 Electron-potential distribution in the linear region (**a**) and close to the anode region where the potential valley is directed towards the surface (**b**)
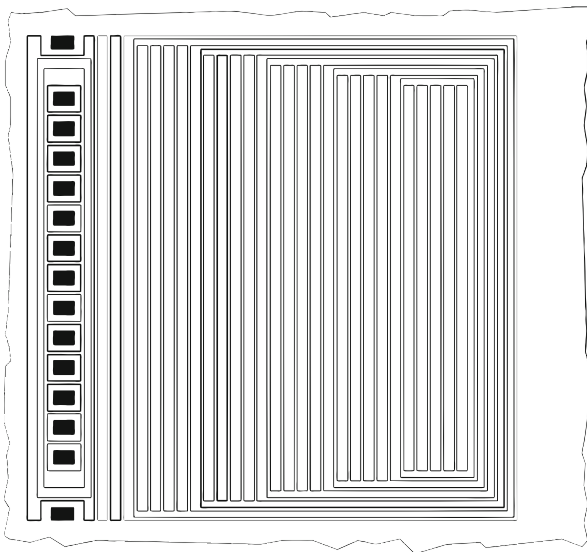
Fig. 5.24 Two-dimensional drift detector with the anode strip divided into pads. The dark pad anodes are embedded in a *p*-doped grid that provides insulation between neighbouring pads

diffusion during the drift time leads to a charge cloud at the anode that is comparable to the spacing of the pads.

For very long drift distances and/or low drift fields, the signal charge will be spread over more than two readout pads. This is an undesirable feature when measuring closely spaced signals. Lateral diffusion can be suppressed by creating deep strip-like p-implanted regions parallel to the nominal drift direction [19]. In this way deviations from the nominal drift direction due to non-uniform doping of the silicon are also avoided.

5.8.2   Radial and Single Side Structured Drift Devices

Radial drift devices are in some sense simpler to design than linear devices because the problem of proper termination of the field-shaping strips does not occur. Radial devices are especially interesting for energy measurement. A small point-like anode with extremely small capacitance may be placed into the centre of the device. The small capacitance results in low electronic noise and as a consequence very good energy resolution.

In one special case radial drift to the outside has been realized with a circular anode divided into pads, thus arriving at two-dimensional position measurement in cylindrical coordinates. An interesting feature of such an arrangement is the high position accuracy at small radius in the azimuthal direction. The position in this second coordinate is obtained from the charge distribution measured in the anode pads by projecting it back in the radial direction. A large-area device of this type [20], with a hole in the centre for the passage of the particle beam, has been produced for the CERES particle physics experiment at CERN. The device also uses a method to drain the current generated at the oxide-silicon interface between the field-shaping rings to an *n*-doped drain contact, separated from the signal-collecting anode [21]. In this manner the anode leakage current is reduced and the measurement precision increased.

The S*ilicon Drift Diode* (SDD) [3] combines radial drift with a homogeneous unstructured backside radiation entrance window (Fig. 5.25). Its principal field of application is in (X-ray) spectroscopy where excellent energy resolution is required. A further significant improvement was obtained by integrating a readout transistor into the device (Fig. 5.26). In contrast to the original drift chamber with the electron potential valley located parallel to the wafer surfaces now only one structured surface provides the drift field in the valley which now is at an angle with respect to the wafer surface.
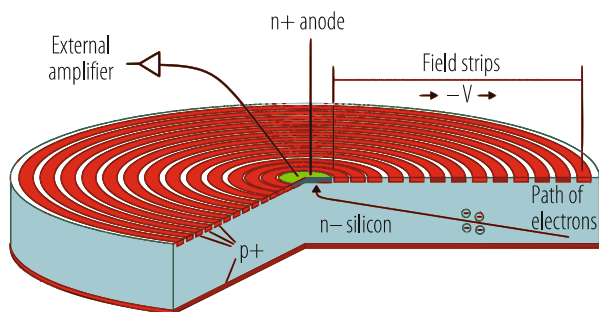
Fig. 5.25 Cylindrical silicon drift detector. The entire silicon wafer is sensitive to radiation. Electrons are guided by an electric field to the small collecting anode in the centre
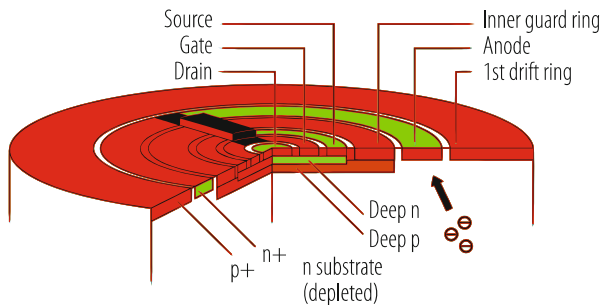
Fig. 5.26 On-chip single sided junction FET coupled to the readout node of a cylindrical silicon drift detector

Having only one surface structured allows using the unstructured surface of the fully depleted device as radiation entrance window. Not having to take other functions into considerations, this radiation entrance window can be made very thin and uniform [22]. The circular geometry with a very small charge-collecting anode in its centre reduces the capacitive load to the amplifier and therefore the noise.

Having the first transistor integrated into the device [23], the capacitance of the detector-amplifier system is minimized by eliminating bond wires between detector and amplifier. In this way stray capacitances between the readout node and ground are avoided, which makes the system faster and less noisy. Further advantages are evident as electrical pickup is significantly reduced and microphony i.e. noise introduced by mechanical vibrations, is excluded. In order to work on the lowly doped and fully depleted substrate, a non-standard "Single Sided Junction Field Effect Transistor" (SSJFET) has been developed [24].

Drift detectors with an integrated transistor are commercially available. They can also be obtained as modules assembled with a Peltier cooler in a gas-tight housing with a thin radiation entrance window (Fig. 5.27). To demonstrate the excellent spectroscopic performance achieved with such devices a spectrum obtained with an ^{55}Fe source and the quantum efficiency are presented in Fig. 5.28 for a cylindrical SDD with a sensitive area of 5 mm^2. The detector temperature, important for the leakage current, was set to $-20\,^\circ$C and the signal shaping time to 1 µs. The Mn$_{K\alpha}$ line at 5.9 keV and the Mn$_{K\beta}$ line at 6.5 keV are clearly separated and their widths are only slightly above the intrinsic Fano limit given by the pair generation process in silicon.

Cylindrical silicon drift diodes with integrated SSJFETs have been manufactured with sensitive areas in the range from 5 mm^2 to 1 cm^2.
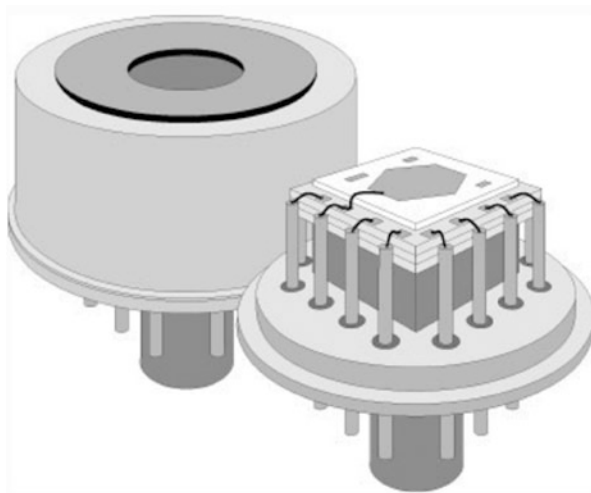
Fig. 5.27 Perspective view of a module consisting of a single-sided structured cylindrical drift detector with integrated SSJFET transistor, cooled by a Peltier element
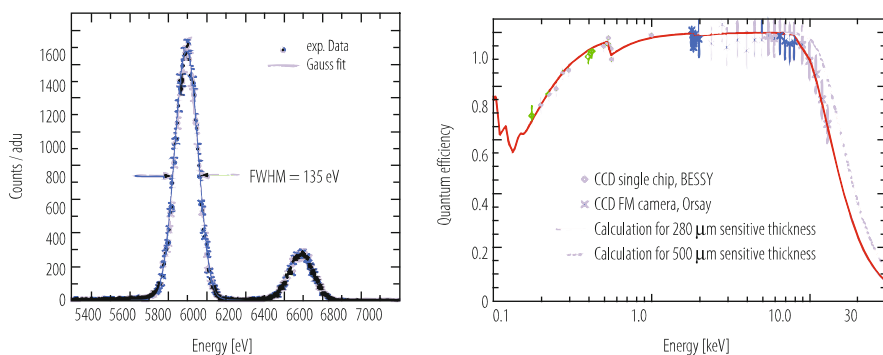
Fig. 5.28 $Mn_{K\alpha}$ – $Mn_{K\beta}$ spectrum (*left*) and quantum efficiency as function of X-ray energy (*right*) of a 5 mm^2 drift diode. The device was operated at -20 °C with a shaping time of 1 μs

5.9 Charge Coupled Devices

Charge coupled devices (CCDs) have for a long time been used as optical sensors, most noticeably as imaging devices in video cameras. Some years ago they also found their application as particle detectors in Particle Physics [25], where specially selected optical CCDs were used. Meanwhile detector systems have been constructed for measuring tracks in electron-positron collisions [26].

p-n CCDs for the special purpose of particle and X-ray detection have been developed [2]. They are based on the principle of side-wards depletion of a double-

diode structure, which is also used in the semiconductor drift chamber. Their first use was in two space-based X-ray telescopes: XMM [27] and ABRIXAS [28].

CCDs are non-equilibrium detectors. Signal charge is stored in potential pockets within a space-charge region, the content of which is then transferred to a collecting readout electrode. In order to retain the thermal non-equilibrium condition, thermally generated charge that also assembles in the potential pockets has to be removed from time to time. Usually this is done during the readout cycle of the device.

While in conventional MOS CCDs minority carriers (electrons in a *p*-type bulk) are collected, the *p-n* CCDs are majority carrier (electrons in an *n*-type bulk) devices. The conventional MOS CCDs to be described in the following for didactic purposes store and transfer the charge directly at the semiconductor-insulator interface. These devices are in practice not used anymore and have been replaced by buried-channel CCDs, in which the store-and-transfer region is moved a small distance away from the surface. As a result they are less sensitive to surface radiation damage. In *p-n* CCDs, this region is moved a considerable distance into the bulk.

5.9.1 MOS CCDs

The CCD transfer mechanism is explained in Fig. 5.29 that shows a cut along the transfer channel. The top part of the *p*-type bulk is depleted of charge carriers and the potential along the Si-SiO$_2$ interface is modulated in a periodic fashion with the help of the metal electrodes on top of the SiO$_2$. Electrons created in the sensitive bulk region assemble in the potential maxima (minima for electrons) at the Si-SiO$_2$ interface.

The charge can now be moved towards the readout electrode by a periodic change of the voltages ϕ_1, ϕ_2, and ϕ_3, as shown in the figure. First ϕ_2 is increased to the same level as ϕ_1 and the signal charge will spread between ϕ_1 and ϕ_2. If now ϕ_1 is lowered, the signal charge will transfer below the electrodes ϕ_2. If this procedure is followed for ϕ_2 and ϕ_3 and then again for ϕ_3 and ϕ_1, the signal charge is transferred by a complete cell. After several cycles the charge will finally arrive at the anode, where it can be measured.

Placing many of these channels next to each other and separating them by so called channel stops one arrives at a matrix CCD. Channel stops prevent the spreading of signal charge to neighbour channels. They can be realized by doping variations as for example an increased *p*-doping between channels. Usually charge is transferred into one additional charge transfer channel oriented perpendicular to the matrix channel (Fig. 5.30) so that the pixel charge can be shifted towards a single output node.
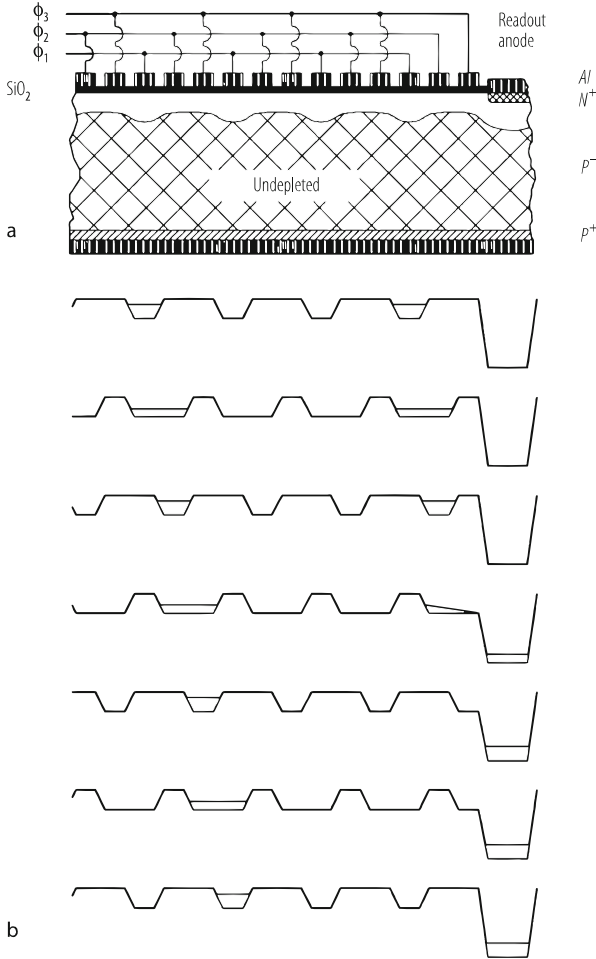
Fig. 5.29 Working principle of a three-phase MOS CCD: layout (**a**); charge-transfer (**b**): Every third gate electrode is connected to the same potential (ϕ_1, ϕ_2, ϕ_3) so that a periodic potential appears below the gates at the Si-SiO$_2$ interface. Electrons are collected in the maxima of the potential distribution. They can be shifted towards the readout anode by changing the potentials, as shown in (**b**)
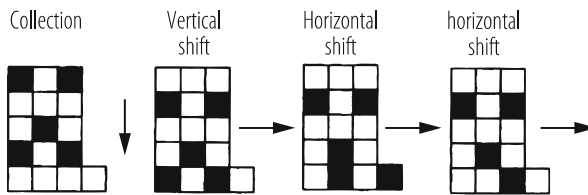

Fig. 5.30 Matrix CCD and the principle of the charge-transfer sequence. Charge is shifted in the vertical direction with all pixels of the matrix in parallel, the lowest row being transferred into a horizontal linear CCD. This horizontal CCD is then read out through a single output node

5.9.2 Fully Depleted pn-CCDs

pn-CCDs were originally developed for X-ray imaging in space. A $6 \times 6 \text{ cm}^2$ size device is used as focal imager in one of the three X-ray mirror telescopes at the European XMM/Newton X-ray observatory [29]. From 2000 until the end of the mission in 2018 it has produced high quality X-ray images of the sky [30].

The *pn*-CCD principle, derived from the silicon drift chamber, has already been shown in Fig. 5.5. The layout of the XMM focal plane detector is shown in Fig. 5.31. Twelve $1 \times 3 \text{ cm}^2$ CCDs with $150 \times 150 \text{ μm}^2$ pixel size are monolithically integrated into a single device placed on a 4 inch silicon wafer of 300 μm thickness. Each column of pixels has its own readout channel allowing for fast parallel readout.

Figure 5.32 shows a cross section of a *pn*-CCD along the transfer channel. Here one sees in greater detail the functioning of the device. Contrary to standard MOS-CCDs the registers are formed as *pn*-junctions and the radiation sensitive oxide plays only a minor role. The device is fully depleted with a higher *n*-type doping concentration in the epitaxial layer below the top surface. This leads to a potential distribution shown in the right part of the figure and prevents holes from the p^+-doped registers to be emitted across the wafer towards the backside *p*-doped entrance window. Charge storage and transfer occurs in a depth of approximately 10 μm in contrast to MOS CCDs where this happens at the $Si-SiO_2$ interface. Fast and efficient charge transfer by drift is therefore possible even for large pixel sizes.
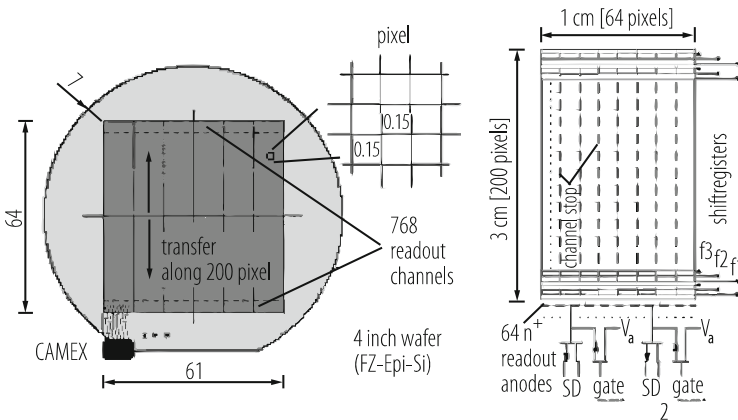
Fig. 5.31 Layout of the XMM *pn*-CCD. 12 logically separate *pn*-CCDs of $1 \times 3 \text{ cm}^2$ area are monolithically fabricated on a 4 in. wafer to a $6 \times 6 \text{ cm}^2$ device with a common backside entrance window. The pixel size is $150 \times 150 \text{ μm}^2$
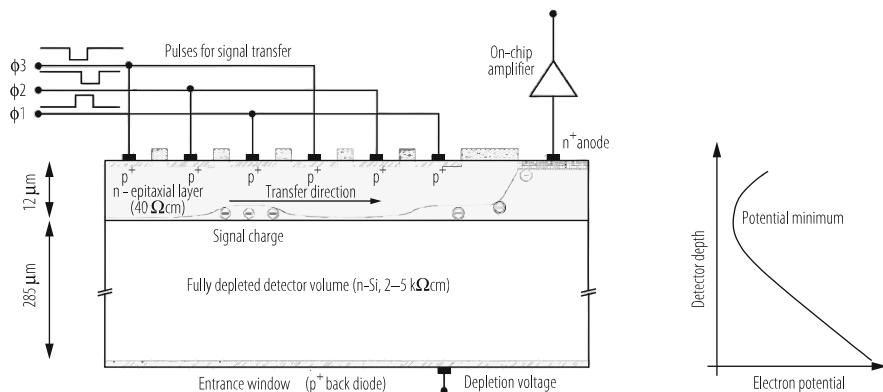
**Fig. 5.32** Cross section through the CCD along the transfer channel

5.9.3 CCD Applications

MOS CCDs have a long history in optical imaging. They have been used in camcorders but also in optical astronomy. In particle physics they were first used by the ACCMOR collaboration in the NA11 experiment at CERN where they were successfully employed for heavy flavour decay detection and measurement. They then found their way to collider physics at SLAC and also to X-ray astronomy, where thinning for backside illumination was necessary to achieve sensitivity for low energy X-rays.

Thinning reduces the sensitive volume and therefore the sensitivity at higher X-ray energies. This disadvantage is avoided with *pn*-CCDs that have a typical thickness of 500 μm and, in addition are built with a ultra-thin entrance window so that high quantum efficiency at both low (100 eV) and high (20 keV) X-ray energies is reached. Good radiation tolerance for X-rays is due to two reasons, the absence of sensitive MOS registers and the absorption of X-rays within the bulk before they reach the sensitive charge transfer region (self-shielding). At XMM/Newton *pn*-CCDs have been operating in space for 18 years without noticeable performance degradation.

Compared to MOS CCDs the readout speed is significantly increased due to the larger pixel size, the higher charge transfer speed and parallel column readout. Very large pixel sizes cannot be realized in MOS CCDs that transfer charges very close to the Si-SiO$_2$ interface.

Use in a further X-ray mission is in preparation: eROSITA (extended ROentgen Survey with an Imaging Telescope Array). Here the CCD is split into an image collecting area and a frame store area. After collection, the complete image is transferred very fast into the frame store area from where it is read with moderate speed row by row while at the same time the next image is collected. The typical image frame readout takes 1 ms, while for MOS CCDs it is in the range of 1 s.
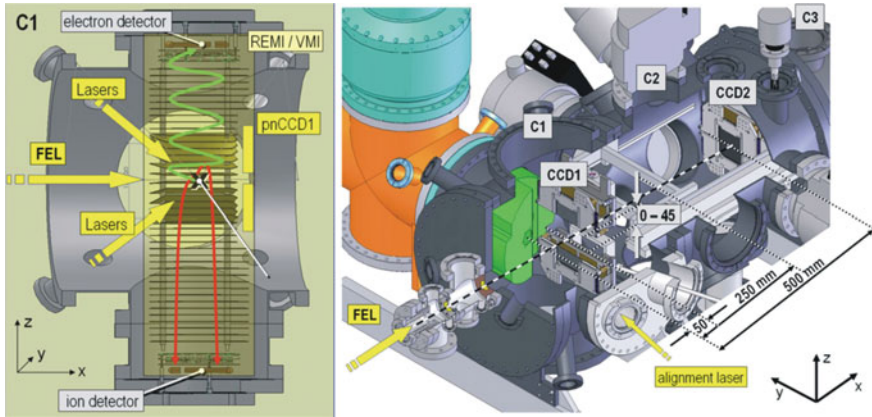
Fig. 5.33 Schematic section through the CAMP detector. The reaction electron and ion detectors with the first CCD sensor plane are depicted on the left hand side. The *pn*-CCD detectors shown in perspective view on the right can detect all photons emerging from the target. In addition, the design allows feeding in other lasers for alignment or pump-probe purposes, as well as for mounting other high-resolution, small-solid-angle electron TOF or crystal spectrometers. The pnCCD1 can be moved in all three directions with a maximum distance of 25 cm along the beam trajectory

Although *pn*-CCDs have been developed for X-ray astronomy they are also visible-light detectors. One application is in adaptive optics that corrects in real time mirror geometries of optical telescopes in order to compensate for atmospheric turbulences at frequencies of approximately 1 kHz.

pn-CCDs are also used in experiments at accelerator-based light sources in particular at X-ray Free Electron Lasers (e.g. FLASH and the European XFEL at Hamburg and LCLS at SLAC). The Center of Free Electron Science (CFEL) in Hamburg has designed the CFEL-ASG Multi Purpose (CAMP) chamber (Fig. 5.33) [31], which combines electron and ion momentum imaging spectrometers with large area, broadband (50 eV to 25 keV), high dynamic range, single photon counting and imaging X-ray detectors based on *pn*-CCDs. The excellent low energy response of *pn*-CCDs has been demonstrated by measuring the response to 90 eV photons at FLASH (Fig. 5.34).

5.10   Active Pixel Detectors

The CCDs discussed in the previous chapter collect charges in pixels during their charge collection period and transport them during the transfer period pixel by pixel to a readout node. Charges produced during the transfer cycle will also be read but the assigned position will be wrong. In active pixel detectors each pixel has its own readout channel and the charge will be assigned to the pixel where it was generated. There are four types of active pixel detectors:
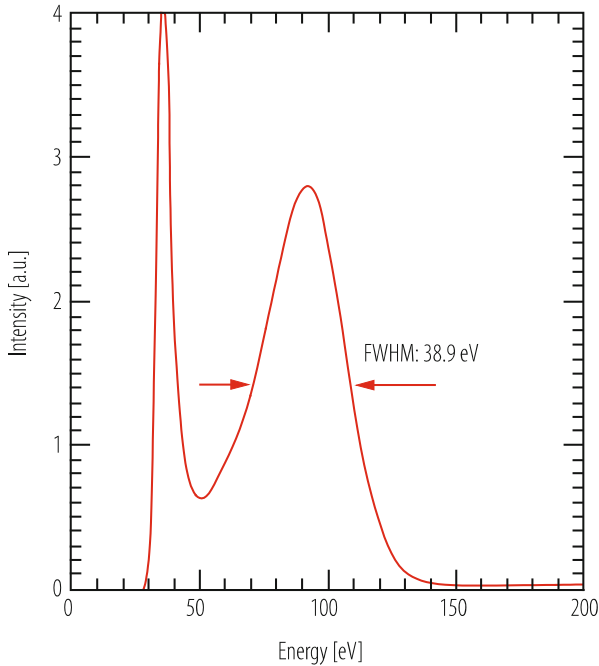
Fig. 5.34 Energy resolution measured at FLASH with 90 eV photons. Every photon generates approximately 25 electron-hole pairs, which are detected with a read-out noise of 2.5 electrons (rms). The measured FWHM energy resolution is only 38.9 eV

(a) Hybrid pixel detectors are diode arrays bonded to an electronics chip produced on a separate wafer so that each pixel has its own readout channel.
(b) MAPS (Monolithic Active Pixel Sensors) are pixel arrays with readout for every pixel directly integrated on the same chip.
(c) DEPFET pixel detectors are two dimensional arrays of DEPFETs with parallel charge collection in the DEPFETs and serial delayed readout of the charges stored in the internal gates.
(d) DEPFET Macro Pixel detectors, pixel detectors with large cell size combine DEPFETs with drift detectors.

All these detector types exist in many variations. Hybrid pixel detectors and MAPS allow parallel data processing and can perform complex tasks thanks to the miniaturized VLSI electronics. This however has a price in power consumption. DEPFET pixel detectors so far are built in a technology of moderately large feature size. Thus complex data processing is not foreseen. Its advantages are sensitivity over the whole bulk, high energy resolution and very low power consumption.

5.10.1   Hybrid Pixel Detectors

Hybrid pixel detectors are used at the Large Hadron Collider (LHC) as the tracking detectors closest to the beam, where the track densities is highest and the radiation exposure most severe. They also became a standard detector for X-ray imaging, in particular at accelerator driven X-ray sources. In their simplest form they consist of a detector wafer with a two dimensional diode array and separate electronics wafers as shown in Fig. 5.35. Every diode is individually connected by bump bonding to its own readout channel. Other connection techniques, including capacitive coupling, have been demonstrated. As readout and sensor are separate, the sensor material can be freely chosen, e.g. a high-Z sensor for the detection of high-energy X-rays.

The main challenge in such a device lies in the electronics that has to provide several functions as for example low noise charge readout and high dynamic range, and—depending on the application—data storage, zero suppression and transmission to the external electronics in analogue or digital form. These functions have to be implemented on an area of the pixel size. Frequently very high speed operation at low power is required as is the case for example in the LHC at CERN. Reaching these goals has been possible by profiting from the dramatic industrial progress in submicron electronics and adapting it to the specific needs. The use of submicron electronics that uses very thin gate oxides has also alleviated the problems with respect to radiation damage.

The typical pixel dimension for the hybrid pixel sensors presently operating at the CERN LHC are of order $100 \times 100\ \mu m^2$. The modules of the ATLAS vertex
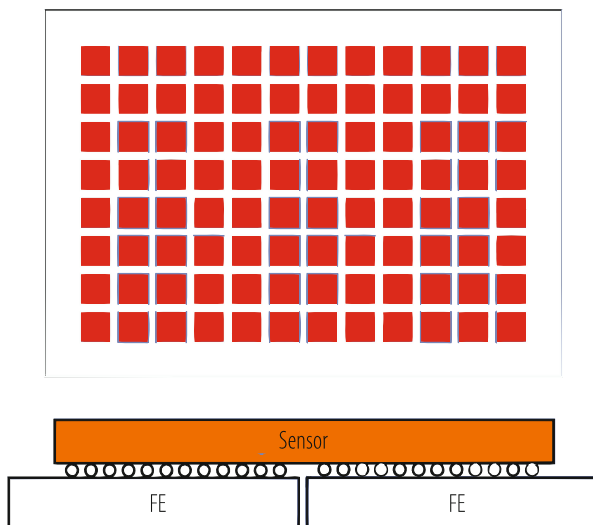
Fig. 5.35 Concept of a Hybrid Pixel Detector consisting of a diode array "flip chip" bonded to several readout chips

**Fig. 5.36** Photo of an
ATLAS pixel detector module
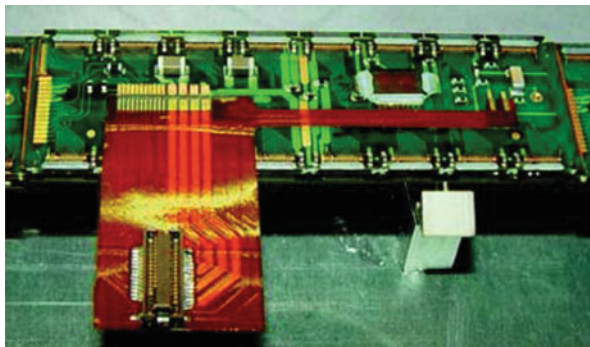
detector, shown in Fig. 5.36, have a pixel size of 50 µm × 250 (400) µm, the ones of CMS 100 µm × 150 µm For the High-Luminosity LHC hybrid pixel detectors with pixel sizes of 50 µm × 50 µm and 25 µm × 100 µm are under development.

The hybrid pixel detectors used for X-ray science face somewhat different challenges and follow different concepts. AGIPD (Adaptive Gain Integrating Pixel Detector) [32], which operates at the European XFEL at Hamburg, where X-rays are delivered in pulse-trains with 220 ns distance between pulses, is designed to detect single and up to 10^4 photons with energies in the range 5–15 keV per pulse in pixels of 200 µm × 200 µm, and store 350 frames to be read out in between the pulse trains. This is achieved by signal-driven switching into four gain ranges. In addition, the 500 µm thick pixel sensor is designed for a breakdown voltage above 900 V for ionizing doses up to 1 GGy. There are many applications in X-ray science, where the recording of individual frames is not required, but the number of hits above a given threshold or in a given energy interval are counted for every pixel or the integrated charge for a given time interval recorded. As the electronics takes significantly less space than required for recording and storing individual frames, pixel sizes as small as 55 µm × 55 µm have been achieved. Outstanding examples for such detectors are PILATUS [33] developed at PSI, and the MEDIPIX series [34], developed by a collaboration centred at CERN.

5.10.2 Monolithic Active Pixel Sensors (MAPS)

This name is used for pixel sensors produced with integrated circuit technology on a single wafer using part of the substrate as detector material. One advantage of MAPS is the significantly easier fabrication of detector modules resulting in a significant cost reduction; another is that MAPS can be produced in CMOS Fabs, which includes a fast turn-around time for the development. However, MAPS are very complex devices and achieving all the requirements of the experiments at high-luminosity, including their radiation performance remains a challenge.
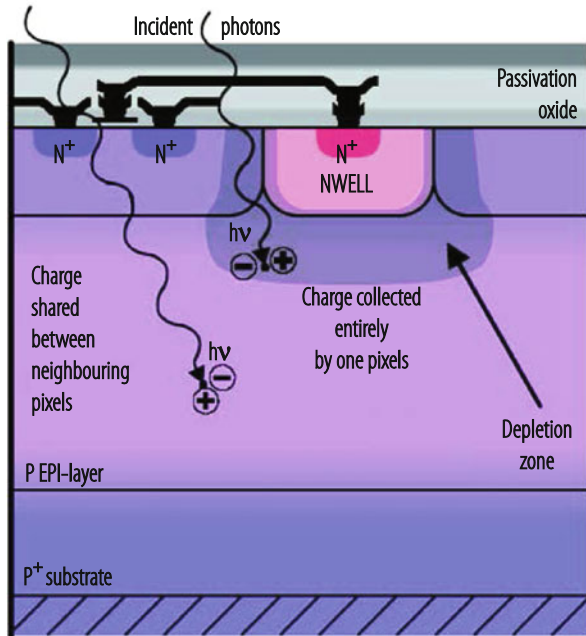
Fig. 5.37 Cross section through a pixel of a MAPS fabricated on CMOS technology but using only NMOS transistors

A first successful demonstration of MAPS operating in an experiment is the EUDET beam telescope [35], with MAPS using only *n*-channel transistors out of an original CMOS technology. Figure 5.37 shows the cross section through a MAPS pixel cell. The *n*-well is used as collecting electrode and all transistors are placed within the *p*-wells. A small volume next to the *n*-well is depleted of charge carriers. In this region signal electrons are collected by drift, but, the major part of the sensitive volume—the *p*-epitaxial layer—is field-free. Thus most of the charge is collected by diffusion, which is intrinsically slow and leads to a large spread of charge into neighbouring cells. There are good reasons why *p*-type transistors are avoided. They would have to be placed into an *n*-well. If this well were separated from the charge collecting electrode it—depending on the *n*-well potentials—would collect signal electrons in competition to the signal electrode or might even inject electrons into the bulk. If it were put into the same well as the collecting electrode it would induce charge directly into the input of the pixel.

For photon detection—as shown in the figure—in addition the material on the top as for example the conducting leads as well as the thick insensitive well zones will absorb part of the incident radiation.

The pixel circuitry (Fig. 5.38) is rather simple. It consists of an NMOS input transistor, a reset transistor and an output select switch. Signal charge is stored at the
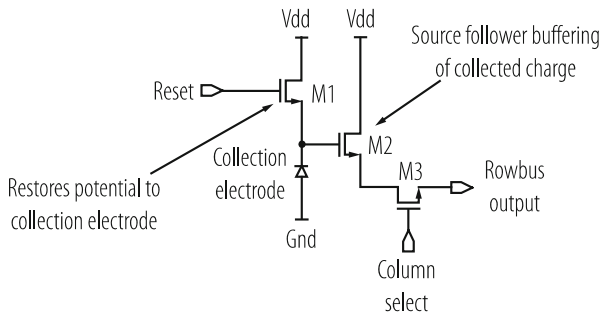
Fig. 5.38 Pixel circuitry of MAPS based on CMOS technology but using only three NMOS transistors. The collecting electrode is directly connected to the gate of a source follower (M2) whose load is common to all pixels of a column and activated by the column select switch. The input node is reset with the reset transistor M1
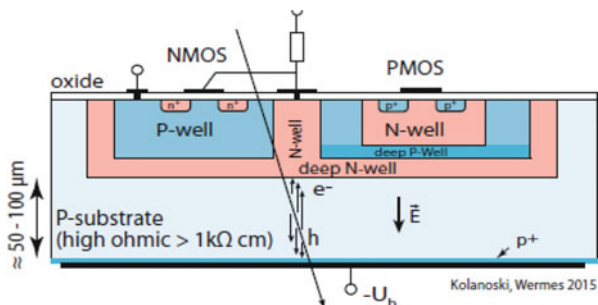
Fig. 5.39 DMAPS with large collection electrodes (figure from Wermes-Kolanoski)
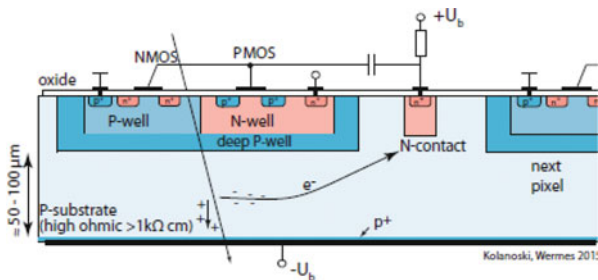
Fig. 5.40 DMAPS with small collection electrodes

input node, read out sequentially and cleared afterwards. MAPS using both CMOS types have also been developed [36].

To overcome the problem of slow charge collection by diffusion, which also makes the sensor sensitive to bulk radiation damage, DMAPS (Depleted CMOS Active Pixel Sensors), are being developed [37]. They are fabricated on substrates with resistivity between 100 Ω·cm and a few kΩ·cm and operated with depletion depths of typically 50–200 μm. As shown in Figs. 5.39 and 5.40, two approaches

are followed: Large Collection Electrode (a) and Small Collection Electrode (b). Design (a) has the advantage of a more uniform electric field resulting in shorter drift distances, and thus a good radiation tolerance is expected. Its disadvantage is the large capacitance of about 100 fF per pixel and an additional well-to-well capacitance of similar value, which results in increased noise, reduced speed, higher power consumption and possibly cross-talk between sensor and digital electronics. Design (b) has a small electrode adjacent to the well in which the electronics is embedded. This has the advantage of a small capacitance of about a few fF and thus improved noise and speed at low power. However, the electric field in the sensor is not uniform with low field regions. This makes them more sensitive to radiation damage. DMAPS of both types have been fabricated by different foundries in 150 nm, 180 nm and 350 nm technologies. They show impressive results even after irradiation with hadrons to fluences exceeding a few 10^{15} cm^{-2}.

5.10.3 DEPFET Active Pixel Sensors

The Depleted Field Effect Transistor structure shown in Fig. 5.6 is a natural building element for a pixel detector. It acts simultaneously as detector and as amplifier. A variety of DEPFET designs can be constructed. Figure 5.41 shows two examples, one with cylindrical, the other with linear geometry.

Arranging many of these devices in a matrix and connecting them in such a way that selected DEPFETs can be turned on, one arrives at a pixel detector with charge
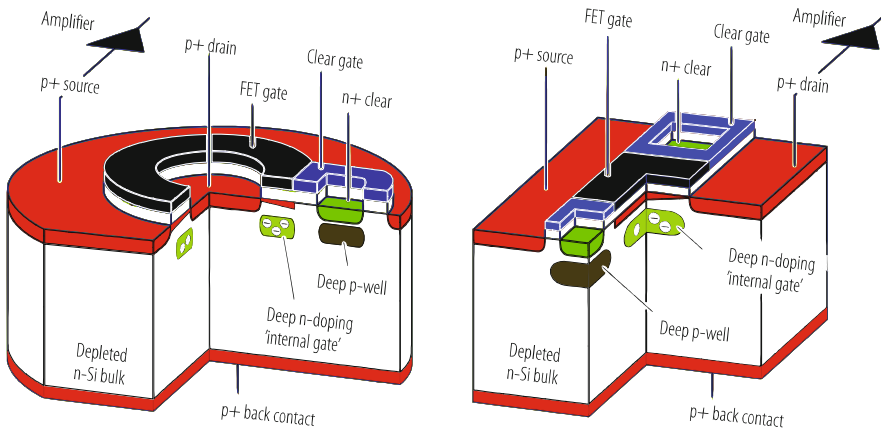
Fig. 5.41 Schematic drawings of MOS-type DEPFETs with circular (*left*) and linear (*right*) geometry. The signal charge is collected in a potential well ("internal gate") below the FET gate, thereby increasing the conductivity of and thus the current in the transistor channel. The collected charges can be drained towards the clear contact by applying voltage pulses to the clear contact and/or the clear gate

storing capability. Before turning to the matrix arrangement the main properties of the DEPFETs are summarised:

- Combined function of sensor and amplifier;
- Full sensitivity the over complete wafer, low capacitance and low noise, nondestructive repeated readout, complete clearing of the signal charge and thus no reset noise.
- Continuous (real time) and integrating (charge storage) operating modes can be chosen.

The signal can be read out either at the source as indicated in the left figure or at the drain as shown in the linear example. With source readout one compensates the increase of channel conduction due to the charge in the internal gate by a reduction of the external gate-source voltage, seen as voltage change of the source. In the drain readout the source potential is kept constant and the drain-current change can be directly observed. An important property in pixel detector applications is the fact that the signal charge collection occurs not only for current carrying DEPFETs but also for those which have been turned off with the help of the external FET gate.

DEPFET pixel sensors have been developed at the MPI Semiconductor Laboratory in Munich for several purposes, as focal sensors of the proposed European X-ray observatory XEUS [38] and as vertex detector for the BELLE-II experiment at KEK in Japan and the proposed International Linear Collider ILC. In XEUS the combined functions of imaging and spectroscopy are of importance, for the vertex detectors the measurement of position of charged tracks is of prime interest. This however has to be done with very high precision (few μm) and at high readout speed. The position measurement requirement in XEUS is not as stringent; it is matched to the expected quality of X-ray imaging. However, highest emphasis is given to spectroscopic quality and quantum efficiency and data readout speed is still large.

As a consequence of these and further requirements circular geometries have been chosen for XEUS and linear ones for the vertex detectors (see Fig. 5.41). The excellent spectroscopic capabilities of DEPFETs can be appreciated from the ^{55}Fe source spectrum taken with a single circular pixel cell (Fig. 5.42).

The DEPFET with its capability of creating, storing and amplifying signal charge is an ideal building block for a pixel detector. A large number of DEPFETs can be arranged in a matrix in such a way as to power selected DEPFETs for reading and clearing the collected signal charge. Figure 5.43 shows a rectangular arrangement of DEPFETs. Their drains are connected column wise while gates and clear electrodes are connected row wise. Each row has its individual readout channel. A row at a time is turned on with the help of the gate voltage while all other DEPFETs have zero current. Charge collection does not require a current within the DEPFET.

Readout can be performed in double correlated mode: Turning on the current with a negative voltage on the gate is followed by a first reading of the current, a clearing of the signal charge in the internal gate with a positive pulse at the clear contact and a second current reading before the current is turned down again and reading is switched to the next row. The difference of first and second current
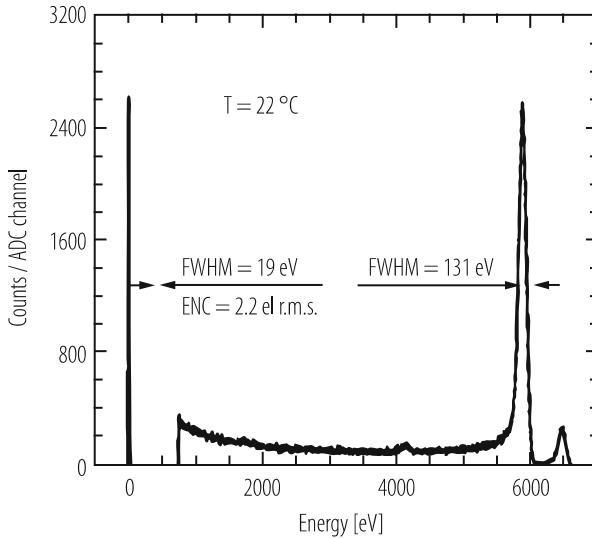
Fig. 5.42 ^{55}Fe spectrum measured with a single circular (XEUS-type) DEPFET. A spectral resolution of 131 eV has been obtained with room temperature operation and 6 μs Gaussian shaping. The separately measured noise peak has a FWHM of 19 eV corresponding to an electronic noise of 2.2 electrons r.m.s
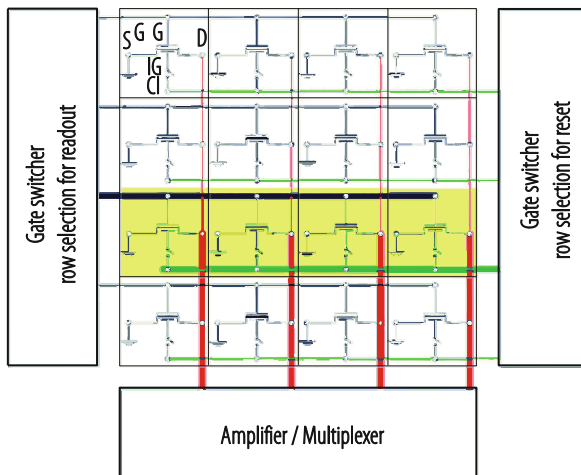
Fig. 5.43 Circuit diagram of a DEPFET pixel detector with parallel row-wise readout of the drain current

reading is a measure for the signal charge in the pixel cell. Alternatively to the procedure described above, sources may be connected column wise and source voltages measured instead of drain currents. Figure 5.44 shows the spectroscopic quality reached with a 64 × 64 DEPFET matrix of 50 × 50 μm^2 pixels.
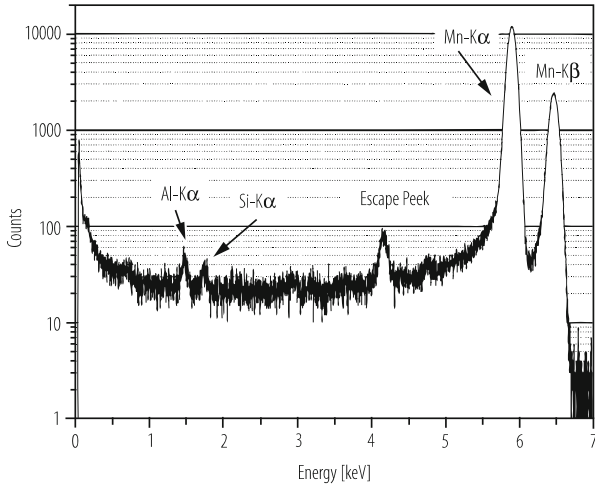
Fig. 5.44 ^{55}Fe spectrum measured at $-28\,^{\circ}$C with a 64×64 cell DEPFET pixel matrix with $50\,\mu$m pixel size

Pixel sensors with large pixels can be constructed by combining DEPFET structure and drift chamber principle. Large pixel may be preferred in order to increase the readout speed and reduce the number of readout channels and power consumption. It is advisable to match the pixel size to the properties of the rest of the system. Over-sampling may increase the electronic noise lead to a worse performance.

Macro Pixel DEPFET Sensors

Figure 5.45 shows the principle with a cut and a top view of a cell. The circular DEPFET structure is located in the centre of a cylindrical drift detector. Electrons created anywhere in the fully depleted bulk are driven by the suitably shaped drift field towards the internal gate below the transistor channel. For this device a new type of DEPFET has been invented that allows clearing of the signal charge with substantially lower voltage by putting the clear electrode inside the drain region located in the centre. The drain region does not consist of a highly doped p region but is formed by an inversion layer that is controlled by a gate voltage and automatically connected to the small drain contact. Putting a sufficiently high positive voltage on this gate, the drain assumes the role of the clear electrode, which is automatically connected to the n-doped clear contact.

Single pixel cells and a 4×4 1 mm^2 pixel matrix (Fig. 5.46) have been tested successfully. Figure 5.47 shows an ^{55}Fe spectrum taken at room temperature. Here one notices a somewhat worse spectroscopic resolution than with the small-pixel devices. This is due to the leakage current which now is collected from a volume which is larger by a factor 400. The leakage current can be suppressed by lowering the operating temperature.
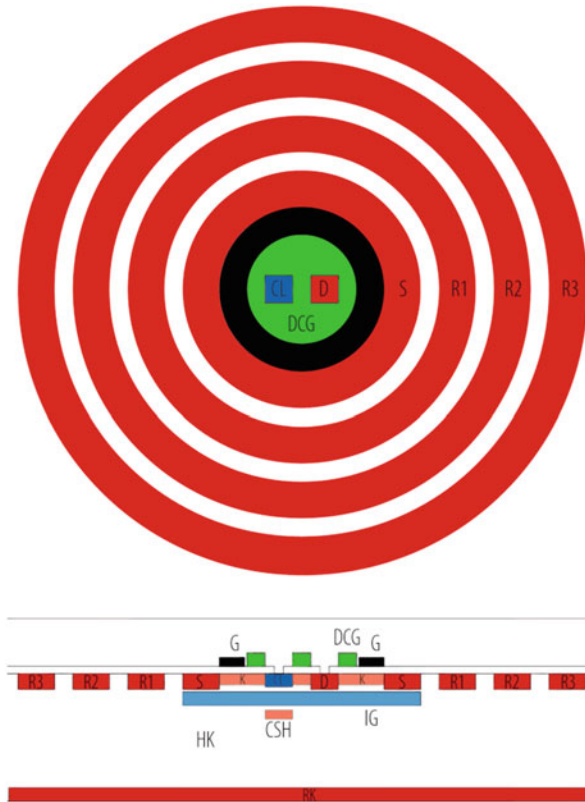
Fig. 5.45 Principle of a macro-pixel cell: A DEPFET located at the centre of a drift detector serves as storage and readout device

New DEPFET Developments

The DEPFET concept allows a variety of further functionalities that have partially been proven experimentally but not yet implemented into a large area pixel detector:

(a) As signal charge is not destroyed by the readout process this charge can be read repeatedly and the measurement precision improves with the square root of the number of measurements. This has been verified with a pair of neighbouring DEPFET transistors arranged in such a way as to allow the transfer of signal charge from one internal gate to the other and in reverse direction. A measurement precision of 0.25 electrons has been achieved independently of the amount of signal charge [39].

(b) Gatable DEPFETs [40] are developed for applications in High Time Resolution Astronomy (HTRA) and Adaptive Optics. They collect signals in preselected time intervals only, whereas the charge generated outside of these gate periods are drained towards a clear electrode.
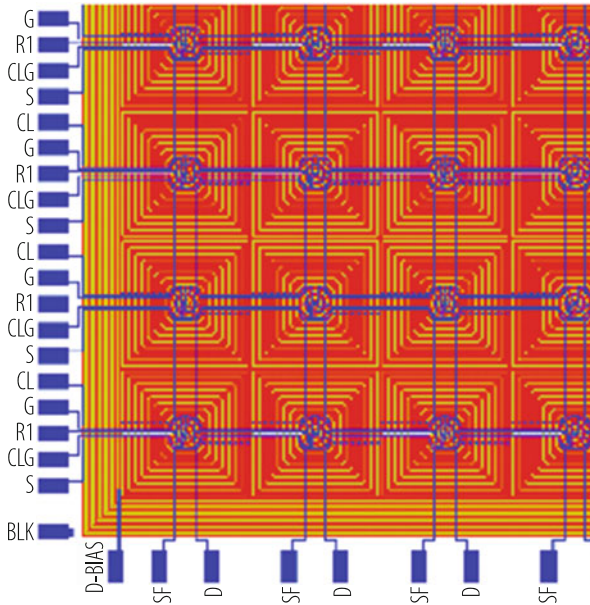
Fig. 5.46 Layout of a macro pixel matrix
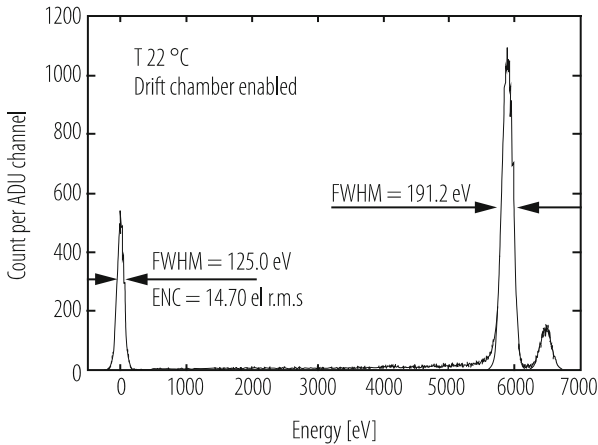
Fig. 5.47 ^{55}Fe spectrum measured at room temperature in a 1×1 mm^2 pixel of an 8×8 macro pixel matrix with 6 μs shaping. The increase of the noise compared to single DEPFET cells is due to the leakage current in the large sensitive volume of $1 \times 1 \times 0.45$ mm^3, which can be reduced by cooling

(c) Nonlinear DEPFETs [41] developed for applications at the European X-ray Free Electron Laser (EuXFEL) at Hamburg. Their non-linear characteristics and high-speed capability combines simultaneously single X-ray-photon sensitivity and very high dynamic range at the 5 MHz EuXFEL repetition rate.

DEPFET Pixel Detector Applications

In the last years DEPFET pixel detectors have been developed at the MPI Semiconductor Laboratory for the following projects:

Bepi Colombo, a mission for observing mercury [42], XEUS/IXO a space based X-ray observatory that will succeed the XMM/Newton and vertex detectors for the International Linear Collider (ILC) and the BELLE-II experiment at the KEK e^+e^- collider.

As an example for the application in X-ray detection Fig. 5.48 shows spectra at high readout rates taken with a Bepi Colombo prototype macro pixel detector. In the final detectors (Fig. 5.49) the pixel size is reduced to $300 \times 300 \, \mu m^2$. An X-ray image obtained by illumination through a mask (Fig. 5.50) demonstrates functioning of the full detector.

The ILC and BELLE vertex detectors [44, 45] require fast readout (10 μs frame time), excellent spatial resolution (5 μm) and minimal material thickness to
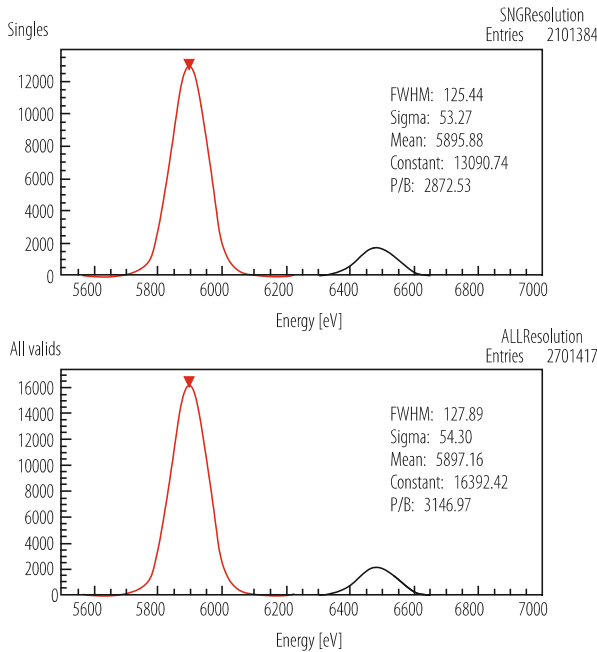
Fig. 5.48 Spectroscopic resolution of Bepi Colombo macro-pixel detectors with 64×64 pixels of $500 \times 500 \, \mu m^2$ size on a 500 μm fully depleted substrate with ultra-thin backside radiation entrance window. The top figure is restricted to photons contained in single pixels. while in the lower part signals split between neighbour pixels are included. Readout was with the ASTEROID pixel chip [43] that averages the DEPFET signals over an "integration time" once before and once after clearing and takes their difference as a measure for the deposited charge. The measured width of 125 eV FWHM with 0.9 μs integration time corresponds to an electronic noise of 4 electrons r.m.s. Reducing the integration time from 0.9 to 0.25 μs increases the width to 163 eV FWHM corresponding to 13 electron charges r.m.s
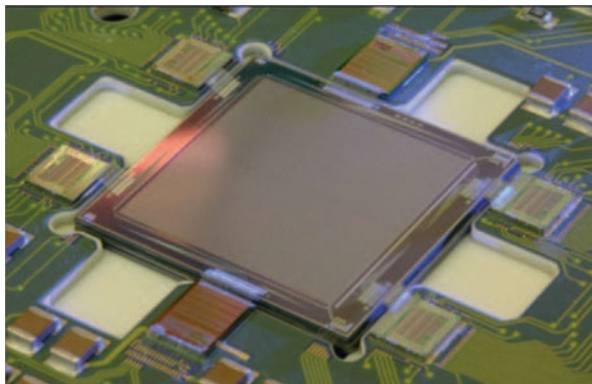
Fig. 5.49 Photo of an assembled macro-pixel detector with two 64 channel ASTEROID readout chips on top and bottom and four steering chips
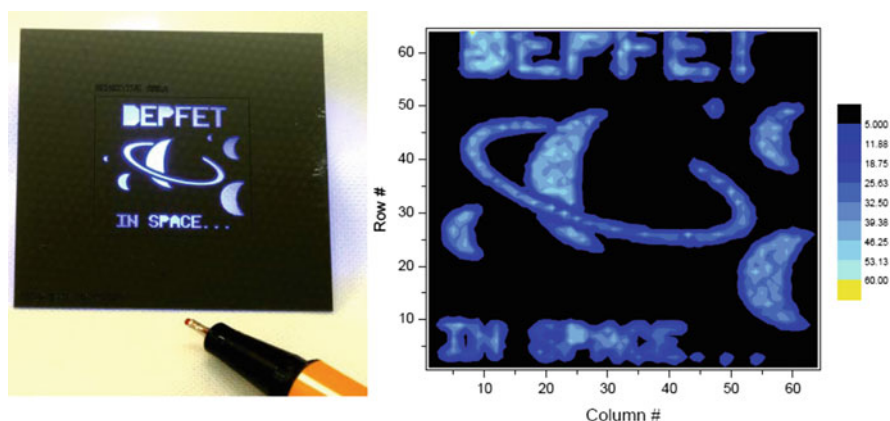
Fig. 5.50 X-ray image (right) obtained with the mask shown on the left

minimize the scattering of charged particles. Consequently the pixel size has been chosen as $25 \times 25 \, \mu m^2$ for ILC and $50 \times 75 \, \mu m^2$ for BELLE-II. A new method for wafer thinning based on wafer bonding technique has been developed in order to produce thin ($50 \, \mu m$) self-supporting all silicon modules [46].

5.11 Detectors with Intrinsic Amplification

Contrary to gas detectors, semiconductor detectors usually provide only the primary ionization as signal charge. This mode of operation is possible because of the low energy needed for producing an electron-hole pair (3.6 eV in silicon, whereas the ionization energy for gases is about 30 eV) and the availability of low noise

electronics. The measurement of the primary ionization without gain avoids any effect of gain variation or amplification noise, and thus leads to stable operation in spectroscopic measurements. However, high speed and very low noise requirements, detection of single photons, compensation for charge losses due to radiation damage or timing accuracies of the order of tens of picoseconds, make an intrinsic amplification of the detectors desirable.

A rather old and well known device is the avalanche diode, with several different operating modes. In the last two decades arrays of avalanche diodes operated in the Geiger mode (SiPMs—Silicon Photo Multipliers) have become photo-detectors of choice for many applications, and more recently tracking detectors with gain (LGAD—Low Gain Avalanche Detectors) are developed with the aim to combine precision position with precision timing in the harsh radiation environment of the high-luminosity LHC at CERN.
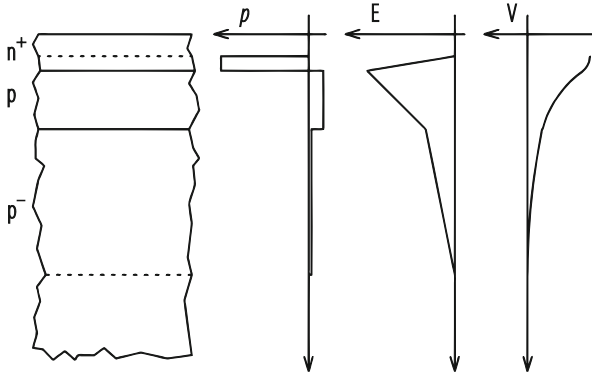
5.11.1 Avalanche Diode

An avalanche diode has a region with a field of sufficient strength to cause charge multiplication. An example of such a device is shown in Fig. 5.51. The base material is low doped p-type silicon. The junction, consisting of a thin highly doped n-type layer on top of a moderately doped p-layer, may also be used as entrance window for radiation, especially when the bulk material is only partially depleted.

An enlarged view of the central top region of Fig. 5.51, in which multiplication takes place, is shown in Fig. 5.52. Also shown are charge density, electric field and potential for the idealized assumption of uniform doping in the n^+-, p- and p^--regions ignoring diffusion. The middle p region is fully depleted and the space-charge region extends into the thin n^+ top region and the low doped p^--bulk. The maximum of the electric field is at the n^+p junction.

Electrons produced below the n^+p junction (and holes produced above the junction) will pass the high field region of the junction when drifting in the electric
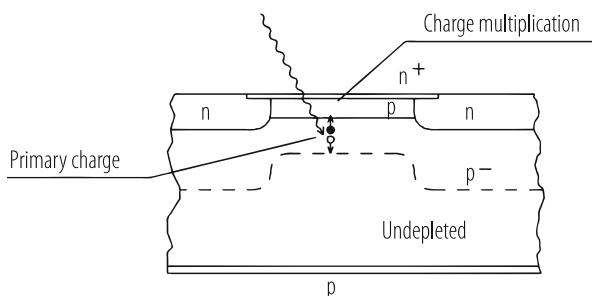
Fig. 5.51 Avalanche diode built on p-type silicon with a high-field region right below the top surface

Fig. 5.52 Amplification region of the avalanche diode shown in Fig. 5.51. Also shown are charge density ρ, electric field E, and potential V

field towards the collecting electrode on top (on bottom). If the electric field is strong enough to accelerate electrons (or holes) between collisions with the lattice imperfections so that the kinetic energy is sufficient to create another electron-hole pair, the charge produced by the primary ionization is amplified.

One important aspect to be considered in designing or operating avalanche diodes is the different behaviour of electrons and holes with respect to charge multiplication. In silicon, the onset of charge amplification for holes occurs at higher electric fields than for electrons. The situation is opposite in germanium, while in GaAs the difference between electrons and holes is comparatively small.

Therefore several working regimes exist that vary depending on the strength and extension of the high electric field region. In the case of silicon one finds: (a) At low electric field, no secondary electron-hole pairs are generated. The device has the characteristics of a simple diode. (b) At higher electric field only electrons generate secondary electron-hole pairs. The amplified signal will be proportional to the primary ionization signal, with some statistical fluctuation from the multiplication process added to the fluctuation in the primary ionization process. (c) At even higher field, holes will also start to generate secondary electron-hole pairs. Secondary electrons generated by holes will again pass through (part of) the amplification region, thereby possibly generating other (tertiary) electron-hole pairs. This avalanche process will continue until it is either stopped by a statistical fluctuation in the multiplication process or by a sufficiently large drop of the externally supplied voltage. This drop may be due to the increased current passing through a bias resistor or an external enforcement by, for example, a feedback circuit. The generation of a large number of free charge carriers in the multiplication region also reduces the electric field strength and therefore decreases charge multiplication in later stages of the avalanche generation. In this operation mode the output signal is no more proportional to the primary charge; however, single photon detection becomes possible.

5.11.2 Low Intensity Light Detection

An optical photon in its primary interaction will create a single electron-hole pair, a charge too small to be detected by standard electronics. However, intrinsic amplification in an avalanche process makes single photon detection possible. The avalanche diode of Fig. 5.51 is such a device. Operation in proportional mode will result in an output signal proportional to the number of (optical) photons, with some statistical fluctuations of the avalanche process added and additional contributions from the non-uniformity of the electric field in the avalanche region. Operation in limited Geiger mode will result in a signal independent of the number of incident photons. The charge signal will be approximately given by the product of the diode capacitance times the difference of the applied voltage and the voltage at which the avalanche process stops.

As the charge multiplication probability is a strong function of the electric field strength, high uniformity over the active area is required and high field regions at the edge of the device have to be avoided by proper design. Edge breakdown is avoided in Fig. 5.51 by the less strongly doped *n* region at the rim. This leads to a space-charge region extending deeper into the bulk and to a reduction of the maximum field.

If the structure of Fig. 5.51 is to be operated in proportional mode (with only electrons multiplying), primary charge produced by radiation entering from the top has to be generated below the high field multiplication region in order to be properly amplified. Therefore for blue light, with its submicron penetration depth, the efficiency is low for this design.

In choosing the width of the depleted region, one has to consider several partially conflicting requirements. Based on noise considerations, this region should be large in order to reduce the capacitive load to the amplifier. The same is required for the detection of deeply penetrating radiation such as X-rays or energetic charged particles. One may even extend the depleted region all the way to the bottom surface. Then the backside *p*-doped surface can also be used as a radiation entrance window. This can be an advantage for low penetrating radiation such as optical photons, since such an entrance window can be made thin. The disadvantage of a large depleted region is the large volume for thermal generation of electron-hole pairs, the electrons being capable of initializing the avalanche process and, depending on the application, a not wanted sensitivity to deeply penetrating radiation.

The electric field configuration in the avalanche region is shown in an idealized way in Fig. 5.52, assuming abrupt doping changes. Such a distribution is not only unrealistic but also far from optimal for proportional operation: Breakdown should be avoided as much as possible which can be achieved by an extended amplification region and lower hole-to-electron multiplication ratios, as is the case for lower fields. Such a design can be realised by suitably doping the avalanche region.

5.11.3 Solid-State Photo Multipliers: SiPMs

In the last decade a new type of avalanche photon detector has reached maturity and is now commercially available, the Solid State Photo Multiplier, also referred to as SiPM (Silicon Photo Multiplier), G-APD (Geiger Mode Avalanche Photo Diode) or MPPC (Multi Pixel Photon Counter) [47]. It consists of two dimensional arrays of 100–10,000 single photon avalanche diodes (SPADs), called pixels, with typical dimension between $(10 \, \mu m)^2$ and $(100 \, \mu m)^2$. The pixels are operated in limiting Geiger mode and every pixel gives approximately the same signal, independent of the number of photons which have produced simultaneously electron-hole pairs in the amplification region of the pixel. The sum of the pixel signals is equal to the number of pixels with Geiger discharges, from which the number of incident photons can be determined. As the output charge for a single Geiger discharge is typically larger than 10^5 elementary charges, 0, 1, 2, and more Geiger discharges can be easily distinguished, enabling the detection of single optical photons with high efficiency and sub-nanosecond timing. The quenching of the Geiger discharge is either achieved by a resistor in series with each pixel or an active feedback.

Two types of SiPMs have been developed: Analogue and Digital. In Analogue SiPMs [47] the individual pixels are connected to a common readout and the SiPM delivers the summed analogue signal. In Digital SiPMs [48] each pixel has its own digital switch to a multi-channel readout system and the output is the digitized pulse height and precise time information for the pixels with Geiger discharges. Digital SiPMs also allow disabling pixels with high dark-count rates.

The pulse shape and the gain of SiPMs are explained with the help of Figs. 5.53 and 5.54: A schematic cross section of a single pixel is shown in Fig. 5.53, and an electrical model of a pixel with resistor quenching, in Fig. 5.54. The bias voltage is denoted V_{bias}, the single pixel capacitance C_{pix}, and the quenching resistance R_q. Frequently, in particular for SiPMs with larger pixel sizes, a capacitance C_q parallel to R_q is implemented. In the quiescent state the voltage over C_{pix} is V_{bias}. When an electron-hole pair in the amplification region starts a Geiger discharge, in the model the switch is closed and C_{pix} is discharged through the current source until the turn-off voltage V_{off} is reached, at which the Geiger discharge stops and the switch opens. The assumption of a constant current source is certainly oversimplified. However the sub-nanosecond discharge time is so short, that details of the time dependence of the discharge current hardly affect the results of the simulation. If a finite capacitance C_q is present, a fast pulse with charge $C_q \cdot (V_{bias} - V_{off})$ appears. After the switch opens, C_{pix} is charged up to V_{bias} with the time constant $\tau \approx R_q \cdot C_{pix}$ and the total signal charge is approximately $(C_{pix} + C_q) \cdot (V_{bias} - V_{off})$. Figures 5.55 and 5.56 show two examples of pulse shapes: (a) For a KETEK SiPM with $(15 \, \mu m)^2$ pixels and negligible C_q, and (b) for a KETEK SiPM with similar doping profiles however with $(50 \, \mu m)^2$ pixels and a finite C_q. The value of R_q has to be sufficiently high to quench the Geiger discharge. As C_{pix} increases with increasing pixel area, $\tau = R_q \cdot C_{pix}$ also increases, and a finite C_q has to be introduced to achieve a good timing performance and an increased pulse height if fast pulse shaping is used.
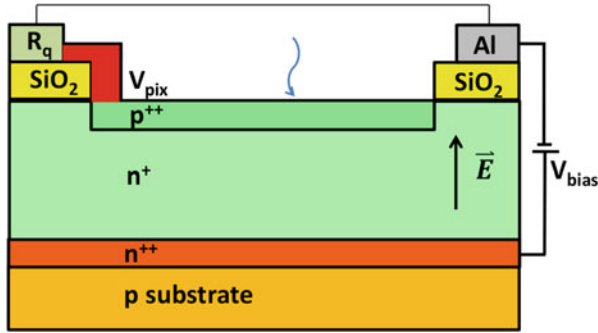
Fig. 5.53 Example of the schematic layout of a SiPM pixel. The Geiger breakdown occurs in the high-field n^+ region, which has a depth of order 1–2 μm. The p^{++}-electrode of every pixel is connected through the quenching resistance (R_q) to the biasing lines (Al) to which the biasing voltage V_{bias} is applied The photons enter through the transparent p^{++}-electrode
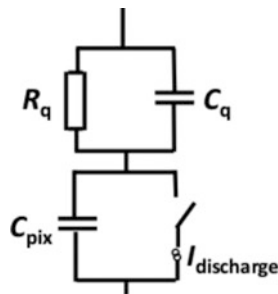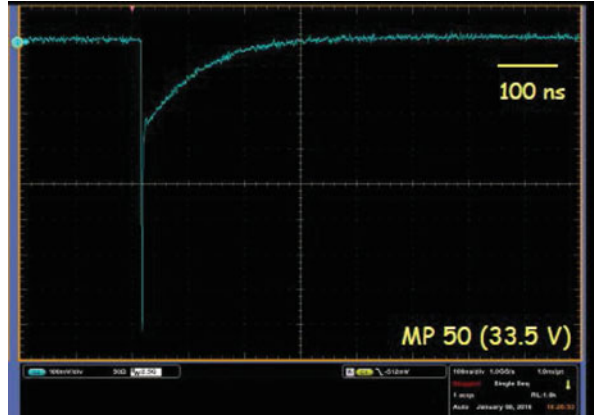

Fig. 5.54 Electrical model of a single SiPM pixel
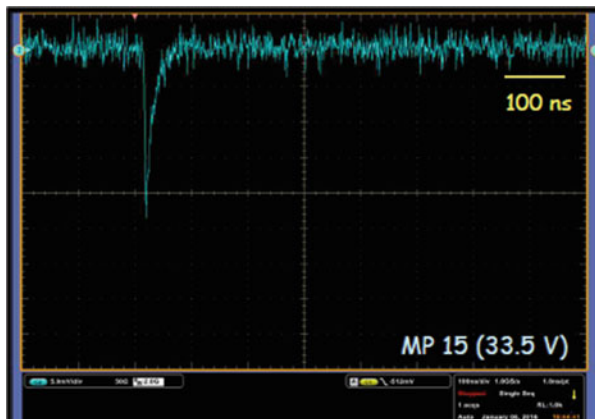
**Fig. 5.55** Pulse shape from a single photon for a KETEK SiPM with 4384 pixels of (15 μm)^2: A single exponential with $\tau = R_q \cdot C_{pix} \approx 20$ ns

Fig. 5.56 Single photon
pulse shape for a KETEK
SiPM with 400 pixels of
$(50\,\mu m)^2$: A prompt signal
due to the finite value of C_q
and a slow component with
the time constant $\tau =
R_q \cdot C_{pix} \approx 110$ ns is observed

In our discussion we distinguish between the breakdown voltage V_{bd}, the threshold voltage for a Geiger discharge, and the turn-off voltage V_{off}, the voltage at which the Geiger discharge stops. Differences $V_{bd} - V_{off}$ of up to about 1 V have been observed [49]. They should be taken into account when characterising or modelling SiPMs. We note that V_{bd} can be obtained from I–V measurements, as the voltage at which the current rises quickly due to the onset of Geiger discharges or the voltage at which the photon detection efficiency starts to differ from zero, and V_{off} can be determined from the dependence of SiPM Gain on V_{bias} by extrapolating the linear Gain(V_{bias}) dependence to Gain = 1.

One outstanding feature of SiPMs is the single-photon resolution, as demonstrated in the charge spectrum shown in Figs. 5.57 and 5.58 [50]. 0, 1, ... up to >30 simultaneous Geiger discharges can be distinguished allowing for straight-forward
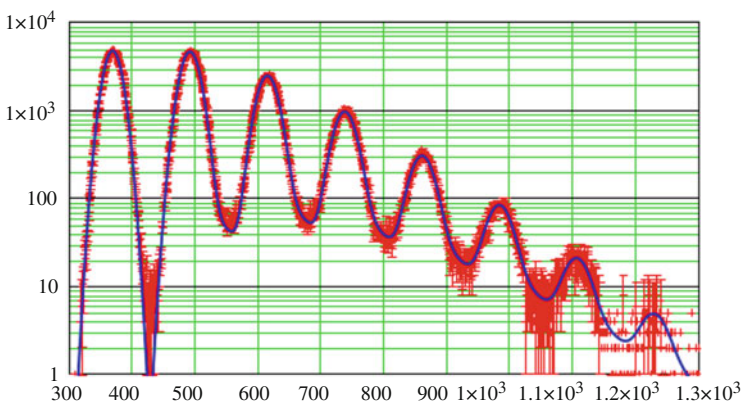
Fig. 5.57 Pulse height spectrum for a pulsed picosecond-laser measured with a KETEK SiPM with 4384 pixels of $(15\,\mu m)^2$. The solid curve is a model fit to the data. The average number of photons producing an initial Geiger discharge is 1.15
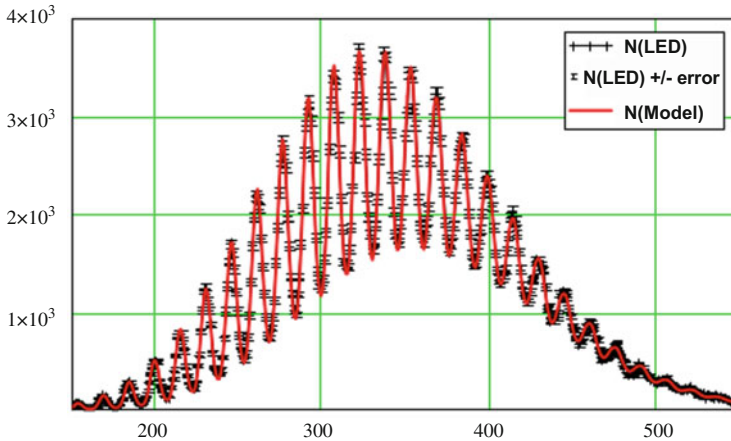
Fig. 5.58 Same as Fig. 5.57, however with an average number of photons producing an initial Geiger discharge of 18.6

calibration methods. The high photon-detection efficiency, where after careful optimisation values in excess of 60 % for wavelengths between 250 and 600 nm have been reached, the high gain of typically 10^6, and the intrinsic timing resolution of a few picoseconds, are other attractive performance parameters. In addition, SiPMs are not affected by magnetic fields, operate in a wide temperature range, are very robust, and work at moderate bias voltages ($\approx$ 25–75 V). Also, thanks to the microelectronics technology, SiPMs have highly reproducible performance parameters and are relatively inexpensive.

Limitations of SiPMs are their size, which is typically below 1 cm^2, and their limited dynamic range, essentially determined by the number of pixels. In addition, the measurement of the number of photons is affected by two sources of excess noise, which worsen the resolution beyond Poisson statistics: After-pulsing and Cross-talk. After-pulses are the result of charge carriers which are produced in the Geiger discharge and trapped in defect states. Depending on the energy in the silicon band gap and the properties of the defect states, they are released with different de-trapping time constants and cause additional signal fluctuations, which depend on the integration time of the readout electronics. In Figs. 5.57 and 5.58, which show pulse-height spectra recorded with a 100 ns gate at room temperature, after-pulses can be seen as entries in-between the peaks. Cross-talk is produced by the photons from the accelerated charges in the Geiger discharge, which generate electron-hole pairs in adjacent SiPM pixels. The photon path can be inside of the silicon but also via reflection in the protective layer of the SiPM or a light guide. This light path is so short that this cross-talk can be considered as prompt. Implementing trenches filled with absorbing material in-between the pixels reduces the prompt cross-talk significantly. The photons from the Geiger discharge can also generate electron-hole pairs in the non-depleted region of the SiPM, which can diffuse into

the amplification region and cause delayed cross-talk. The result of prompt cross-talk is that the number of entries in the peaks does not follow a Poisson distribution, even if the number of photons causing initial Geiger discharges does. As shown in [51] the result of cross-talk is that the number of entries in the peaks follows a Generalised-Poisson instead of a Poisson distribution. We note that the solid curve shown in Figs. 5.57 and 5.58 is the result of a model fit which includes both after-pulsing and prompt cross-talk simulated by a Generalised Poisson distribution. The model provides a fair description of the measurements and gives a precise determination of the SiPM parameters [50]. As both, after-pulses and cross-talk are related to the number of charge carriers in the Geiger discharge and thus to the Gain, the corresponding probabilities are expected to be approximately proportional to $V_{bias} - V_{off}$, which is also observed. Typical values at $V_{bias} - V_{off} = 5$ V for after-pulsing as well as prompt cross-talk are 5 % resulting in an excess noise factor, the ratio of the square of the relative resolution to the Poisson expectation, ENF $= [(\sigma_{meas}/mean_{meas})/(\sigma_{Poisson}/mean_{Poisson})]^2$ of ≈ 1.08. As the photon detection efficiency increases with voltage and finally saturates, whereas Gain and ENF continue to increase, there is a voltage at which the photon number measurement is optimal.

Dark counts are another limitation of SiPMs. Typical dark count rates (DCR) for SiPMs before irradiation are between 10 and 100 kHz/mm^2 at room temperature. Cooling reduces the DCR by about a factor 2 for an 8 °C reduction in temperature. Ionizing radiation, which mainly causes damage to the SiO_2, hardly affects the DCR. However non-ionizing radiation, like neutrons or high energy (> 5 MeV) particles, significantly affect the performance. At sufficiently high fluences (Φ) the DCR is so high that most pixels are in a state of Geiger discharge, the photon-detection efficiency decreases and finally the SiPM stops working as a photo-detector. Whereas V_{bd} and the electrical SiPM parameters hardly change up to $\Phi = 5 \times 10^{13}$ cm^{-2}, DCR increases by many orders of magnitude: For a KETEK SiPM with 15 µm pitch at –30 °C and $(V_{bias} - V_{off}) = 5$ V, DCR increases from ≈ 10 kHz/mm^2 before irradiation to ≈ 200 GHz/mm^2 after irradiation by reactor neutrons to $\Phi = 5 \times 10^{13}$ cm^{-2} [52, 53]. It is found that the increase in DCR is approximately proportional to Φ. It is also observed that after irradiation the increase of DCR with excess voltage is significantly steeper and the decrease with temperature slower after than before irradiation. As a result of the increased DCR, the signal baseline shows large fluctuations and single photon detection becomes impossible. Finally the occupancy of the pixels by dark counts is so high that the probability of a photon hitting a pixel which is already busy increases and the photon detection efficiency degrades. For the KETEK SiPM with 15 µm pitch at –30 °C the photon detection efficiency due to dark counts is reduced by a factor 2 for $\Phi = 5 \times 10^{13}$ cm^{-2} at $(V_{bias} - V_{off}) \approx 2.5$ V, and essentially zero for $\Phi = 5 \times 10^{14}$ cm^{-2} [53]. At these high fluences the dark currents exceed several tens of mA and thermal run-away has to be avoided.

After irradiation a significant reduction of DCR by annealing occurs. Annealing is a strong function of temperature: The typical reduction of DCR is a factor 2–3 after several days at room temperature, and a factor 10–50 at 175 °C. A systematic

study of different annealing scenarios, which allows to optimise the temperature cycling for operating SiPMs in high radiation fields, as available for silicon tracking detectors without gain [7, 10], is so far not available. In [54] it is demonstrated that SiPMs produced by Hamamatsu and SENSL, after irradiation to a fluence of 10^{14} cm^{-2} and annealed at 175 °C can achieve single photon detection at 77 K with a DCR below 1 kHz/cm^2.

The values of V_{bd} and V_{off} have a temperature dependence of order 20 mV/°C, which results in a temperature-dependent gain. However this is not a real problem and several feedback systems for gain stabilisations have been designed and are used.

Due to the vast application potential, which spans from research, over industrial applications to medicine, several firms develop and manufacture SiPMs. In close collaboration with research institutions, in particular working in particle physics, a rapid development and major improvements of SiPMs are presently under way.

5.11.4 Ultrafast Tracking Detectors: LGADs

At the HL-LHC (High-Luminosity Large Hadron Collider at CERN planned to start operation in 2026) in the large collider experiments ATLAS and CMS there will be on average ≈ 200 interactions with vertices distributed over ≈ 10 cm along the beam direction for every bunch crossing. For the complete kinematic reconstruction of the most interesting interactions in a bunch crossing, the information of the individual detector components has to be assigned to the correct interaction vertices. To illustrate the problem, Fig. 5.59 shows the reconstructed tracks extrapolated to the interaction region for a single bunch crossing with 50 interactions recorded in 2012. For a few vertices the interaction times, which are spread over ≈ ±200 ps, as obtained from a simulation, are given. For an efficient assignment of tracks to vertices, tracking detectors with high efficiency, 5 μm position resolution, 20 ps

Fig. 5.59 Interaction times of a number of proton-proton vertices in a single bunch crossing with 50 interactions [55]. The data have been recorded by the CMS experiment in 2012. At the HL-LHC, the average number of interactions per bunch crossing is expected to be about 200
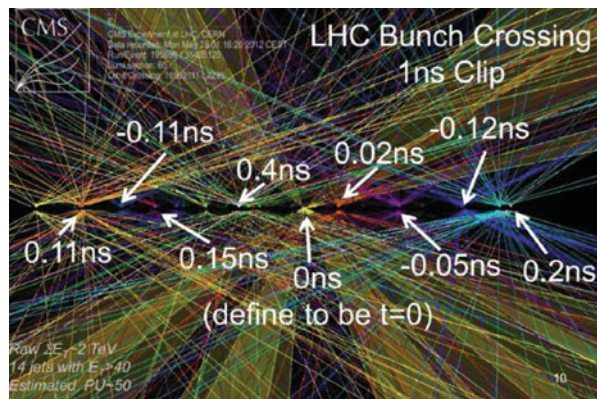
timing accuracy and 25 ns pulse shaping, are required. From simulations [55] it is concluded that pixel sensors with 50 μm active thickness and a doping profile similar to the one shown for APDs in Fig. 5.52 and operated at a gain of $\approx$ 20 can reach the required performance. These detectors are called Low-Gain-Avalanche Detectors, LGADs.

Different to optical photons which generate single electron-hole pairs, minimum-ionizing produce about 75 charge pairs per micro-meter and a high gain is not required. In addition to increasing fluctuations, high gain causes also practical difficulties and increases the shot noise from the dark current. Thin sensors have the additional advantage of smaller dark currents and a pulse rise time which increases with decreasing sensor thickness.

The effects which influence the timing accuracy can be grouped in five categories: (1) Position-dependent fluctuations of the charge carriers produced by the charged particle to be measured, (2) excess noise of the amplification mechanism, (3) position dependent drift field and coupling of the of the drifting charges to the readout electrodes, (4) electronics noise, and (5) digitisation error of the time-to-digital convertor.

A major issue for LGADs is the control of the gain after irradiation. The change of the effective doping by dopant removal and defect states, and the decrease of the mobilities and amplification coefficients of electrons and holes due to radiation damage appear to present major problems. These are addressed in an extensive R&D program which started in 2012 and has already given first encouraging results.

5.12 Summary and Outlook

Different concepts of solid silicon sensors and the electronics required for their readout have been described in this contribution. Although a detailed theoretical understanding of silicon devices had already been achieved in the 1960s, silicon detectors remained a niche application, used mainly in Nuclear Physics. This changed around 1980, when Josef Kemmer adapted the planar technology of micro-electronics to sensor fabrication and the ACCMOR Collaboration demonstrated the reliable long-term operation and excellent physics performance of silicon strip detectors. Based on these results, many groups started to develop and use silicon detectors, and today there is hardly a particle physics experiment, which does not rely heavily on them. The areas covered by silicon detectors in the particle physics experiments increased from tens of cm^2 to hundreds of m^2. Large areas of silicon detectors are even used on satellites for space experiments. In parallel to silicon detectors, the development of low-noise ASICs and connection technology started. They are required for reading out the more and more complex silicon sensors. In addition, a number of industrial producers, in closed collaboration with academia, developed and fabricated silicon sensors. Today silicon radiation detectors are a quite big market. Initially developed for Particle Physics, the use of silicon detectors spread into many different fields of science, medicine and industrial applications.

Since 1980 several new detector concepts were proposed, realised and used for a variety of measurement tasks. Outstanding examples are drift detectors, fully depleted CCDs, DEPFETs, MAPSs 3-D sensors, APDs and SiPMs. The different devices have their advantages and shortcomings, but offer high-performance solutions for most measurement tasks. In recent years radiation damage for the use of silicon sensors at high flux or high luminosity colliders has become more and more of a concern. Whereas radiation damage by X-rays can be controlled by a proper sensor design, the question up to which fluence of high-energy radiation silicon detectors can be used is a field of intense research. Unfortunately other sensor materials, like crystalline diamond or GaAs seem not to be a solution. Defect engineering, by doping crystals with different impurities has resulted in some improvements. However, a breakthrough for high fluences could not be demonstrated. Therefore the only approach appears to optimise the sensor layout for radiation tolerance. The recipe followed are high fields and low charge collection distances. How far intrinsic amplification can help remains an open question. For the design optimisation, complex TCAD (Technology Computer-Aided Design) simulations are performed. In spite of some first successes, a major progress is still required. As far as the electronics, which is exposed to the same fluences, is concerned, the sub-micron technology with nano-meter dielectric layers resulted in a big step in radiation tolerance.

For the future there is the strong hope that detectors can be fabricated which achieve the challenging performance parameters in the high radiation fields of the HL-LHC and future high-luminosity colliders. The field of solid state detectors will also profit very much from the ongoing industrial R&D efforts, in particular of 3-D integration technology and nano-electronics. Last but not least I very much hope that, like in the past, radically new ideas will come up and expand further the applications of solid state detectors.

References

1. E. Gatti, P. Rehak: *Semiconductor Drift Chamber - An Application of a Novel Charge Transport Scheme*, Nucl. Instrum. Meth. 225 (1984) 608-614; E. Gatti et al.: *Silicon Drift Chambers - First results and optimum processing of signals*, Nucl. Instrum. Meth. 226 (1984) 129-141; E. Gatti et al.: *Semiconductor Drift Chambers*, IEEE Trans. Nucl. Sci. 32 (1985) 1204-1208.
2. L. Strüder et al.: *The MPI/AIT X-ray imager (MAXI) - high speed pn-CCDs for X-ray detection*, Nucl. Instrum. Meth. A 288 (1990) 227-235; L. Strüder et al.: *First results with the pn-CCD detector system for the XMM satellite mission*, Nucl. Instrum. Meth. A 326 (1993) 129-135; L. Strüder et al.: *A 36 cm² large monolythic pn-charge coupled device X-ray detector for the European XMM satellite mission*, Rev. Sci. Instrum. 68 (1997) 4271-4274.
3. J. Kemmer, G. Lutz: *New semiconductor detector concepts*, Nucl. Instrum. Meth. A 253 (1987) 356-377.
4. J. Zhang et al.: *Study of radiation damage induced by 12 keV X-rays in MOS structures built on high-resistivity n-type silicon,* Journal of Synchrotron Radiation 19 (2012) 340-376.
5. T. Poehlsen, et al.: *Charge losses in segmented silicon sensors at the Si-SiO2 interface*, Nucl. Instrum. Meth. A 700 (2013) 22-39.

6. J. Schwandt et al.: *Design and First Tests of a Radiation-Hard Pixel Sensor for the European X-Ray Free-Electron Laser,* IEEE TRANSACTIONS ON NUCLEAR SCIENCE, VOL. 61, NO. 4, AUGUST 2014 1894-1901.

7. M. Moll: *Displacement Damage in Silicon Detectors for High Energy Physics*, Manuscript accepted for Publication in IEEE Transactions on Nuclear Science, DOI:https://doi.org/10.1109/TNS.2018. 2819506.

8. V. Eremin, E. Verbitskaya, Z. Li: *The origin of double peak electric field distribution in heavily irradiated silicon detectors,* Nucl. Instrum. Meth. A 476 (2002) 556-564.

9. R. Klanner et al.: *Determination of the electric field in highly-irradiated silicon sensors using edge-TCT measurements,* Nucl. Instrum. Meth. A 951 (2020) 162987.

10. R. Wunstorf et al.: *Results on Radiation Hardness of Silicon Detectors up to Neutron Fluences of* $10^{15} n/cm^{-2}$, Nucl. Instrum. Meth. A 315 (1992) 149-155.

11. S.I Parker, C.J. Kenney and J. Segal: *3D - A proposed new architecture for solid state radiation detectors*, Nucl. Instrum. Meth. A 395 (1997) 328.

12. J. Kemmer et al.: *Experimental confirmation of a new semiconductor detector principle*, Nucl. Instrum. Meth. A 288 (1990) 92-98.

13. M. Caccia et al.: *A Si Strip Detector with Integrated Coupling Capacitors*, Nucl. Instrum. Meth. A 260 (1987) 124-131.

14. C. Cottini, E. Gatti, G. Gianelli, G. Rozzi: *Minimum noise preamplifiers for fast ionization chamber*, Nuovo Cimento (1956) 473-483.

15. E. Gatti, P.F. Manfredi: *Processing the signals from solid state detectors in elementary particle physics*, Rivista di Nuovo Cimento 9, Ser. 3 (1986) 1-145.

16. W. Buttler et al.: *Low-noise, low power monolithic multiplexing readout electronics for silicon strip detectors*, Nucl. Instrum. Meth. A 273 (1988) 778-783.

17. P. Jarron, et al.: *Deep submicron CMOS technologies for the LHC experiments*, Nucl. Phys. B Proc. Suppl. 78, no. 1-3 (1999) 625-634.

18. P. Rehak et al.: *Semiconductor drift chambers for position and energy measurements*, Nucl. Instrum. Meth A 235 (1985) 223-234.

19. A. Castoldi et al.: *A new drift detector with reduced lateral diffusion*, Nucl. Instrum. Meth A 377 (1996) 375-380.

20. W. Chen et al.: *Large area cylindrical silicon drift detector*, IEEE Trans. Nucl. Sci. 39 (1992) 619-628.

21. P. Rehak et al.: *Spiral silicon drift detectors*, IEEE Trans. Nucl. Sci. 36 (1989) 203-209.

22. R. Hartmann, et al.: *Ultrathin entrance windows for silicon drift detectors*, Nucl. Instrum. Meth. A 387 (1997) 250-254.

23. R. Hartmann et al.: *Design and test at room temperature of the first silicon drift detector with on-chip electronics*, IEDM Technical Digest (1994) 535-539.

24. V. Radeka et al.: *Implanted silicon JFET on Completely Depleted High Resistivity Devices*, IEEE El. Dev. Lett. 10, nb. 2 (1989) 91-95; E. Pinotti et al.: *The pn-CCD On-Chip Electronics*, Nucl. Instrum. Meth. A 326 (1993) 85-92.

25. R. Bailey et al.: *First Measurements of Efficiency and Precision of CCD Detectors for High Energy Physics*, Nucl. Instrum. Meth. 213 (1983) 201-215; C.J.S. Damerell et al.: *CCDs for Vertex Detection in High Energy Physics*, Nucl. Instrum. Meth. A 253 (1987) 478-481; C.J.S. Damerell et al.: *A CCD based vertex detector for SLD*, Nucl. Instrum. Meth. A 288 (1990) 236-239.

26. K. Abe et al.: *Design and performance of the SLD vertex detector: a 307 Mpixel tracking system*, Nucl. Instrum. Meth. A 400 (1997) 287-343.

27. D.H. Lumb et al.: *X-ray Multi-Mirror Mission - an overview*, SPIE 2808 (1997) 326-337.

28. G. Richter et al.: *ABRIXAS, A Broadband Imaging X-ray All-sky Survey*, (L. Bassani, G. di Cocco, eds.): Imaging in High Energy Astronomy, Experim. Astron. (1996) 159.

29. N. Meidinger et al.: *The PN-CCD detector for XMM and ABRIXAS*, SPIE 3765 (1999) 192-203.

30. L. Strüder et al.: *pnCCDs on XMM-Newton – 42 months in orbit*, Nucl. Instrum. Meth. A 512 (2003) 386-400.

31. L. Strüder et al.: *Large format, high-speed, X-ray pnCCDs combined with electron and ion imaging spectrometers in a multipurpose chamber for experiments at 4th generation light sources*, Nucl. Instrum. Meth A614 (2010) 483-496.
32. B. Henrich et al.: *The adaptive gain integrating pixel detector AGIPD: A detector for the European XFEL*, Nucl. Instrum. Meth. A 633 (2011) S11-S14; A. *Allahgholi et al.*: *The adaptive gain integrating pixel detector*, JINST 11 (2016) C02066.
33. B. Henrich et al.: *PILATUS: A single photon counting pixel detector for X-ray applications*, Nucl. Instrum. Meth. A 607 (2009) 247-249.
34. R. Ballabriga, M. Campbell, X. Llopart, *ASIC Developments for radiation imaging applications: The medipix and timepix family*, Nucl. Instrum. Meth. A 878 (2018) 10-23.
35. W. Dulinski et al.: *Beam telescope for medium energy particles based on thin, submicron precision MAPS*, in: Nuclear Science Symposium Conference Record, 2007, NSS '07, IEEE, Vol. 2, 995-1002.
36. L. Ratti et al., *CMOS MAPS with fully integrated, hybrid-pixel-like analog front-end electronic*, eConf C0604032 (2006) S.0008.
37. I. Peric, *A novel monolithic pixelated particle detector implemented in high-voltage CMOS technology*, Nucl. Instrum. Meth. A 582 (2007) 876-885; I Peric et al.: *High-voltage pixel detectors in commercial CMOS technologies for ATLAS, CLIC and Mu3e experiments*, Nucl. Instrum. Meth. A 731 (2013) 131-136.
38. XEUS Astrophysics working group: *X-ray Evolving - Universe Spectroscopy - The XEUS scientific case*, ESA SP-1238 (1999), 30 pages.
39. S. Wölfel et al.: *Sub electron noise measurements on repetitive non-destructive readout devices*, Nucl. Instrum. Meth. A 566 (2006) 536-539.
40. G. Lutz, R.H. Richter, L. Strüder: *Halbleiterstruktur, insbesondere in einem Halbleiterdetektor, und zugehöriges Betriebsverfahren*, EU Patent 1 873 834; G. Lutz, et al.: *DEPFET detector-amplifier structure: Properties, achievements and new developments, concepts and applications*, in: Nuclear Science Symposium Conference Record, 2007, NSS '07, IEEE, Vol. 2, 988-994.
41. G. Lutz, L. Strüder: *DEPFET Transistor mit großem Dynamikbereich und Halbleiterdetektor*, DE Patent 10 2007 048 890; G. Lutz et al.: *DEPFET Sensor with intrinsic signal compression developed for use at the XFEL free electron laser radiation source*, Nucl. Instrum. Meth. A 624 (2010) 528-532.
42. J. Treis et al,: *DEPFET based instrumentation for the MIXS focal plane on BepiColombo*, in: Instrumentation and Methods for Astrobiology and Planetary Missions XII (R.B. Hoover, G.V. Levin, A. Yu Rozanov, K. Retherford, eds.), Proc. SPIE 7441 (2009) 774116.
43. M. Porro et al.: *Performance of ASTEROID: A 64 channel ASIC for source follower readout of DEPFET matrices for X-ray astronomy*, IEEE Nuclear Science Symposium Conference Record 2008, pp. 1830-1835.
44. R.H. Richter et al.: *Design and technology of DEPFET pixel sensors for linear collider applications*, Nucl. Instrum. Meth. A511 (2003) 250-256.
45. L. Andricek et al.: *The MOS-type DEPFET pixel sensor for the ILC environment*, Nucl. Instrum. Meth. A 565 (2006) 165-171.
46. L. Andricek, G. Lutz, M. Reiche, R.H. Richter: *Processing of ultra-thin silicon sensors for future e^+e^- linear collider experiments*, IEEE Trans. Nucl. Sci. 51 (2004) 1117-1120.
47. D. Renker: *Geiger-Mode Avalanche Photodiodes, history properties and problems*, Nucl. Instrum. Meth. A 567 (2006) 48-56; D. Renker and E. Lorenz: *Advances in solid state photon detectors*, JINST 4 (2009) P04004.

48. T. Frach et al.: *The Digital Silicon Photomultiplier – Principle of Operation and Intrinsic Detector Performance*, in: Nuclear Science Symposium and Medical Imaging Conference Record (NSS/MIC), N34-4 (2012) 1959-1965; C. Degenhardt et al.: *The digital Silicon Photomultiplier – A novel sensor for the detection of scintillation light*, in Proceeding to IEEE NSS-MIC conference, Orlando U.S.A. October 25–31 2009, Proc. IEEE 2009 (2009) 2383-2386; S. Mandai, E. Charbon: *Multi-channel digital SiPMs: concept, analysis and implementation*, in: Nuclear Science Symposium and Medical Imaging Conference Record (NSS/MIC), N34-4 (2012) 1840-1844.
49. V. Chmill et al.: *Study of the breakdown voltage of SiPMs*, Nucl. Instr. Meth. A 845 (2017) 56-59.
50. V. Chmill, et al.: *On the characterisation of SiPMs from pulse-height spectra*, Nucl. Instr. Meth. A 854 (2017) 70-81.
51. S. Vinogradov: *Analytical models of probability distribution and excess noise factor of solid state photomultiplier signals with crosstalk*, Nucl. Instrum. Meth. A 695 (2012) 247-251.
52. Yu. Musienko et al.: *Radiation damage studies of silicon photomultipliers for the CMS HCAL phase I upgrade,* Nucl. Instr. Meth. A787 (2015) 319–322; Yu. Musienko et al.: *Effects of very high radiation on SiPMs*, Nucl. Instr. Meth. A824 (2016) 111-114.
53. M. Centis Vignali et al.: *Neutron irradiation effect on SiPMs up to* $\Phi = 5 \times 10^{14}$ cm^{-2}, Nucl. Instr. Meth. A912 (2018) 137.
54. M. Calvi et al.: *Single photon detection with SiPMs irradiated up to 10^{14} cm^{-2} 1-MeV-equivalent neutron fluence*, arXiv:1805.07154 (2018).
55. N. Cartiglia et al.: *Tracking in 4 dimensions*, Nucl. Instr. Meth. A845 (2017) 47-51.